Thesis

End-to-End model for free-space-optical Air-to-Space communication services

Wieger Helsdingen

Supervisors
Rudolf Saathof (TU Delft)
Remco den Breeje (AirbusDSNL)

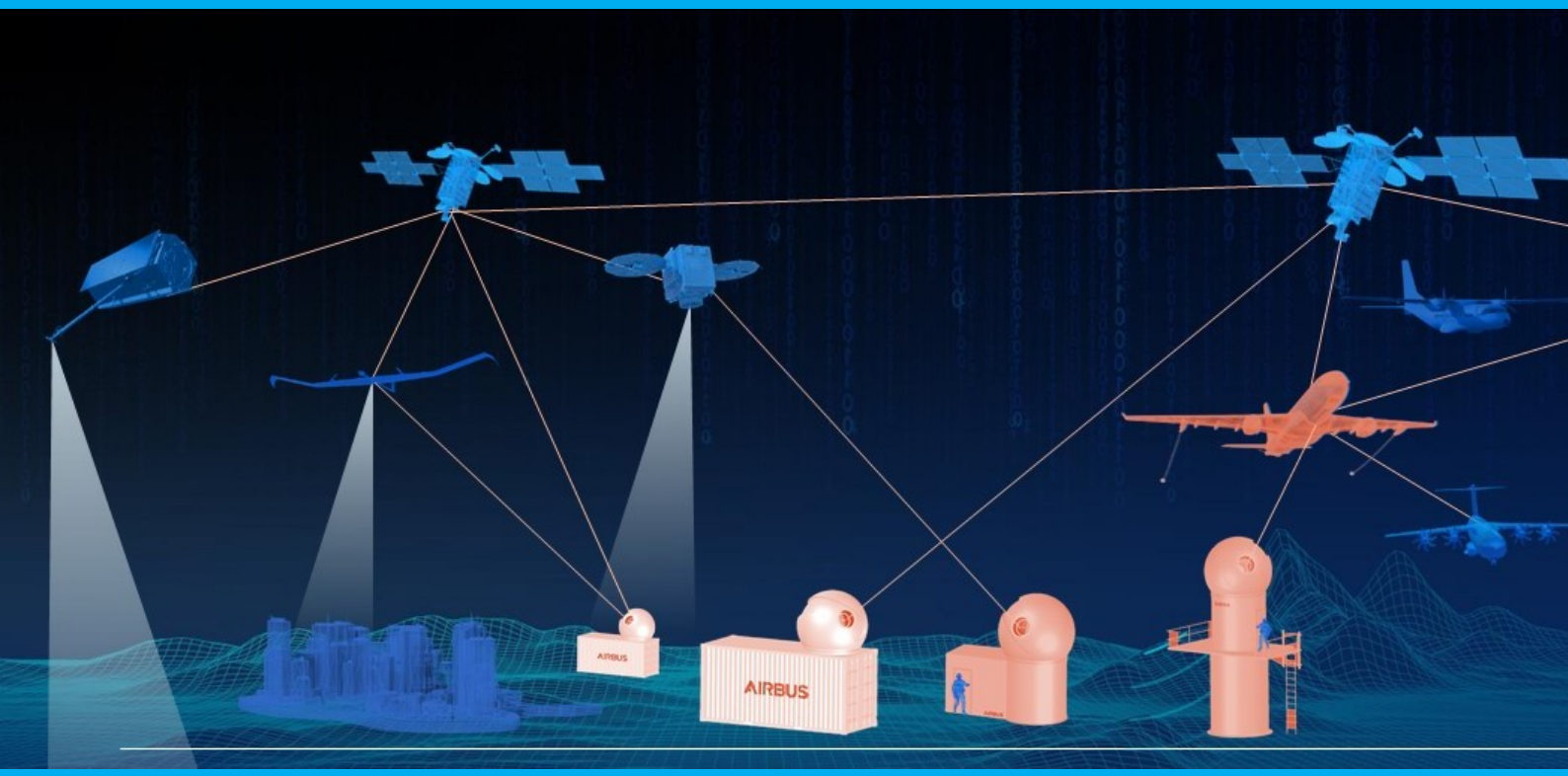

TU Delft AIRBUS

Thesis

End-to-End model for free-space-optical Air-to-Space communication services

by

Wieger Helsdingen

to obtain the degree of Master of Science
at the Delft University of Technology,
to be defended publicly on Wednesday August 17, 2023.

Student number:	4547101	
Project duration:	Octobre 1, 2022 – August 17, 2023	
Thesis committee:	Dr. S. M. Cazaux,	TU Delft, chairman
	Dr. ir. R. Saathof,	TU Delft, supervisor
	Dr. ir. D. Dirkx,	TU Delft, external
	ing. R. den Breeje,	Airbus Netherlands, external

TU Delft

Contents

List of Figures

List of Tables

List of Acronyms

2-PPM	2-ary pulse position modeling.
AC	aircraft.
ADS-B	automatic dependent surveillance broadcast.
AoA	angle-of-arrival.
APD	Avalache photo-diode.
ASL	air-to-space links.
ATS	Acquisition and Tracking System.
BER	bit-error-rate.
bps	bits per second.
BPSK	Binary phase-shift keying.
CDF	cumulative density function.
CGMCM	Coarse-grained Monte Carlo method.
DD	direct-detection.
DLR	Deutsches Zentrum für Luft- und Raumfahrt.
ECI	Earth-Centered-Inertial.
FEC	forward error coding.
FFT	fast-Fourier transform.
FOR	field of regard.
FSO	Free-space-optics.
GEO	geostationary orbit.
GSL	ground-to-space links.
HMM	Heterogeneous multi-scale method.
HV	Hufnagel-Valley.
ISA	international standard atmosphere.
ISL	inter-satellite-links.
KIODO	Kirari's Optical Downlink to Oberpfaffenhofen.
LCT	laser communication terminal.
LEO	low-earth orbit.
LLA	latitude, longitude, altitude.
LOS	line-of-sight.
MEO	medium-earth orbit.
MMM	Modified multi-scale method.
OGS	optical ground stations.
OOK	On-Off keying.
OOK-NRZ	On-Off keying non-return to zero.
OSI	Open Systems Interconnection.
PDF	probability density function.
PIN	Diode with a P-type & N-type semiconductor and a Intrinsic semiconductor in between.
PPM	M-ary Pulse position modeling.
PSD	power spectral density.
PVGeT	Power Vector Geneneration tool.
Q	Quality factor.
RAAN	right ascension of the ascending node.
RAM	random access memory.
RF	radio-frequency.
RMS	root mean square.
RS	Reed Solomon.
RSS	root sum square.
RX	the receiver terminal.
SC	spacecraft/satellite.
SDA	Space Development Agency.
SNR	signal-to-noise.
TLE	two-line element.
TPCWM	Time-parallel compound wavelet method.
TX	the transmitter terminal.
WFE	wave front error.

Introduction Thesis

Free-space-optics (FSO) satellite communication technology currently is a growing area of interest due to its large benefits compared to the currently used radio-frequency (RF) satellite communication technology, such as low latency, high channel capacity, high security, and low mass and power constraints [1]. Numerous potential applications are speculated in [2], such as deep-space communication, data relay in geostationary orbit (GEO) and low-earth orbit (LEO) constellation services. The last application is highly relevant as it has the potential to greatly improve high internet speeds and global connectivity. Optical constellations are already planned to be operational [3, 4, 5, 2, 6]. Modeling FSO communication missions with satellite constellations in LEO will prove helpful for the exploitation of this service.

However, the scope of such missions is naturally very large with many physical processes occurring at high frequencies, from nanoseconds to milliseconds, and low frequencies, from minutes to hours. Considering a 2 hour mission with 2 Gbps data rate, modeling all processes at the lowest time scale would require 1.4 $\mathbf{10^{13}}$ evaluations, indicating the need for a model that can efficiently integrate these processes. Several studies have been performed to model the combined processes of atmospheric turbulence, slow atmospheric variations and platform vibrations [7, 8, 9, 10, 11]. Other studies also include bit detection processes [12, 13, 14]. However, these models are constrained to a static link and thus leave out the lower-frequency processes, such as the platform dynamics (e.g. aircraft and satellite motion). Additionally, link budgets are often used, which leave out much microscopic information.

Therefore, the aim of this thesis is to develop an end-to-end model that is able to simulate the performance of an FSO communication mission with a LEO satellite constellation end-to-end by efficiently combining all the relevant physical processes. A MMM is proposed, based on the Heterogeneous multi-scale method (HMM) [15] and the Time-parallel compound wavelet method (TPCWM) [16]. The MMM is applied to the specified mission in three main steps. First, all performance metrics are defined. Then sub-models are developed to model these performance metrics. Finally, all sub-models are fitted in the MMM, such that it can simulate a solution of the metrics at mission level.

This thesis is performed from October 2022 until August 2023 as a collaboration between the TU Delft (Space flight track) and Airbus Netherlands. The thesis is initiated by the UltraAir program, which concerns the development of an FSO communication service between aircraft and satellites [17]. Therefore, a mission between one aircraft and a satellite constellation is chosen as use case during this research. The main contributions of this thesis are:

- An end-to-end model that allows preliminary analysis and verification of the performance of global FSO communication missions with satellite constellations.
- Insightful analysis into a combined process of multiple physical phenomena at different time scales.

The thesis is written as a scientific paper. The appendix contains all supporting work and additional information that is not included in the scientific paper but is relevant for the thesis. It consists of three main parts. The first part is the scientific article in chapter 1, 2, 3, 4 and 5. The second part consists of the appendices in Appendix A, B, C, D. The third part contains the conclusion and recommendations of the thesis.

Abstract

FSO satellite communication enables data transfer at high bandwidths, low latency, and high security. Due to these benefits, FSO communication services with satellite constellations can hugely improve global connectivity and bandwidth, while maintaining sufficient security.
Modeling a global FSO satellite communication service is beneficial for gaining insight into, and performing preliminary analysis on such missions. However, these missions are complex problems with several physical processes occurring at different time scales. Macroscopic processes in the order of minutes to hours consist of relative platform dynamics (eg. aircraft and satellite motion) and atmospheric attenuation. Microscopic processes consist of atmospheric turbulence- and platform disturbances in the order of milliseconds and transporting photons/bits in the order of nanoseconds. To our knowledge, there are currently no end-to-end models that accurately and efficiently simulate a combination of all these processes.
To overcome this, a multi-scale method is proposed that simulates and combines the physics of the microscopic and macroscopic processes of a global FSO satellite communication mission. A bi-directional air-to-space link is chosen as a use case.
The proposed model simulates a 1.5 hours communication mission in 6 minutes with 8 Gb random access memory (RAM). Platform dynamics and jitter are the most dominant effects. Including microscopic processes results in a performance difference in signal power of 10 dB to 80 dB depending on the strength of the atmospheric channel.
Using the multi-scale method, we can efficiently and realistically simulate an FSO communication service end-to-end between an aircraft and a satellite constellation.

Chapter 1

Introduction

Global capacity demand of 240 Tbits per second (bps) is estimated in the near future [4], increasing each year by 50% according to Nielsen's law of internet bandwidth [18]. FSO satellite communication services can contribute much to global coverage and high capacity, making it highly relevant with this rapidly increasing demand in mind. Additionally, compared to current satellite RF communication, FSO technology has significant benefits with respect to capacity, latency, cost, mass and security [1]. Because of this, FSO satellite communication is a growing area of interest [2] among researchers and models have been developed that evaluate the performance of ground-to-space links (GSL) [12, 13, 7, 19, 20, 8], air-to-space links (ASL) [21] and inter-satellite-links (ISL) [22].

Modeling a global FSO satellite communication service will prove beneficial for the exploitation of FSO technology, as it provides insight into the physics and performance of such large-scale missions. However, these services are complex problems with several physical processes occurring at different orders of frequency. (1) Relative platform dynamics vary within a time scale of hours. (2) A link selection process is required in between each link, occurring every 5 to 10 minutes for LEO constellations. (3) Then, within each link period, slow-atmospheric variations (cloud motion and attenuation) also occur within the scale of minutes (4) Atmospheric turbulence and (5) platform disturbances (vibrations) typically occur in the region of 1 to 100 milliseconds [7, 23]. Finally, considering a multi-Gbps throughput, (6) transportation and processing of photons/bits occur at a nanosecond time scale. With a defined threshold of 1 Hz, processes 1,2 & 3 are macroscopic and processes 4, 5 & 6 are microscopic.

In literature, models are developed that accurately analyze link channels with atmospheric turbulence, attenuation and platform vibrations [7, 8, 10, 11]. More complete link models also include the transported bit processes [12, 13, 14]. However, these models are constrained to a static link and thus leave out the lower-frequency processes of platform dynamics and link selection. Additionally, link budgets are often conveniently used for approximate analysis [13, 14], leaving out valuable information from the microscopic processes.
In order to overcome the challenge of combining the defined processes of a global FSO satellite communication mission, a MMM is proposed, based on the HMM and the TPCWM. Each process is simulated with a sub-model, after which they are integrated using the MMM. This study focuses on the use case of ASL communication missions with bi-directional links. However, a modular and versatile model is built to enable extension to other use cases.

To start modeling and integrating all processes, the physical problem with all corresponding time scales is first described in section 2.1. Then, potential applications of ASL missions are identified, along with the mission drivers to determine important constraints and performance metrics for input and output variables in section 2.2. With the physical domain in mind, the MMM is proposed, based on a trade-off, and described in section 2.3. The application of the MMM on the specified problem is described

in section 2.4. Then, the numerical implementation is explained on sub-model level, and a verification strategy is described in chapter 3. The model is simulated with a selected mission scenario and the results are analyzed in chapter 4, after which a comparison is made with similar methods and experimental data in section 4.3.

Chapter 2

Theory & Method

2.1 Problem description

The physical problem encompasses a global FSO communication service between one aircraft (AC) and a spacecraft/satellite (SC) constellation. It is narrowed down to the lowest communication layer as defined by the Open Systems Interconnection (OSI) model, which is the physical layer [24]. An FSO signal (or laser) connection is modeled between the transmitter terminal (TX) and the receiver terminal (RX). Both uplinks and downlinks are considered in the model, as well as the communication phase and the acquisition phase, as described on page 14 of [25] and visualized in Figure 2.1. During the acquisition phase, both terminals are calibrating their pointing systems with respect to each other to start communication.

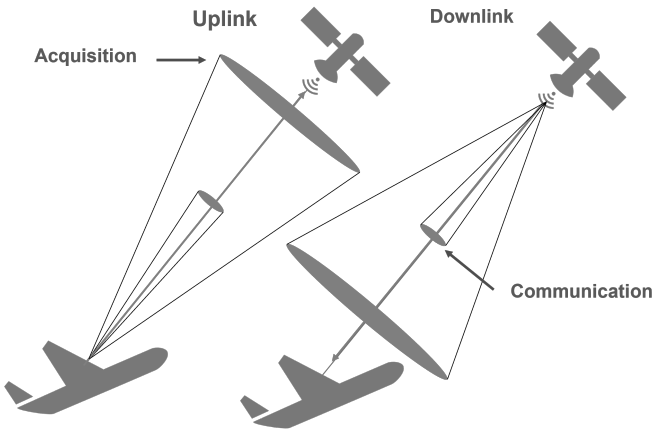

Figure 2.1: Graphical overview of the types of FSO links that are considered in this problem

The problem is divided into orders of time scales of the physical processes in Figure 2.2. The time scale of platform dynamics is determined by the SC orbital period and AC trajectory. The link selection process depends on the link duration, which typically ranges between 5 to 10 minutes for LEO satellites [26]. Slow atmospheric effects are caused by clouds, molecules and aerosols, which are dominated by atmospheric wind speeds varying in a time scale of minutes.

Atmospheric turbulence typically occurs within a scale of 1 to 50 milliseconds [7]. Platform vibrations depend on the spectrum of the vehicle's mechanical vibrations, typically ranging between 1 ms and 100 ms. Other vibrational effects are considered much smaller and are neglected in this study. All physical processes concerning bits are determined by the data rate. Considering links higher than one Gbps leads to a time scale in the order of nanoseconds. Bit processing includes (de)modulation, (de)interleaving and (de)coding.

All processes are conveniently divided into four levels: Mission level, link level, channel level and bit level. Processes at mission level and link level (above 1 Hz) in Figure 2.2 are macroscopic. Processes at channel level and bit level (below 1 Hz) are microscopic. These levels are used as a basis for the numerical model, further discussed in section 2.4.

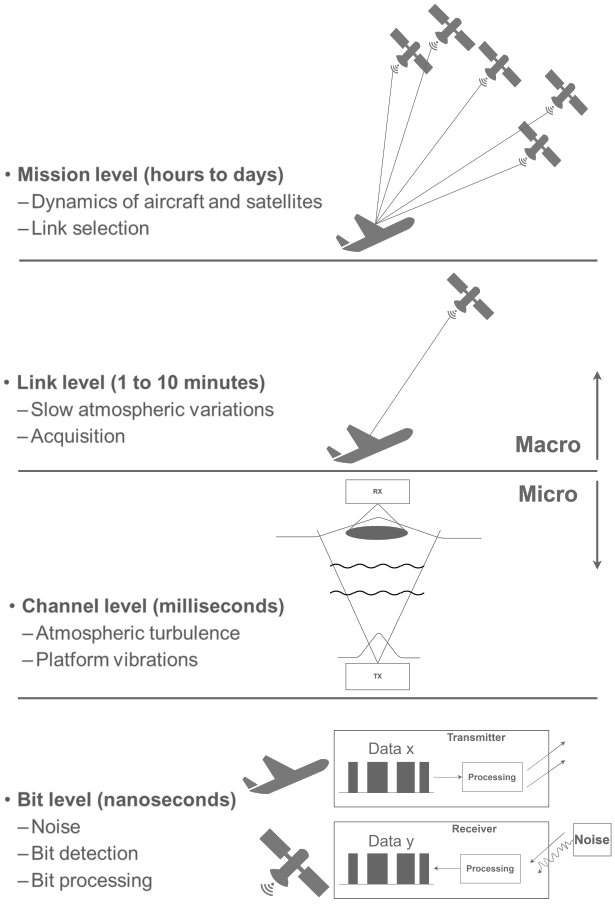

Figure 2.2: Graphical overview of the physical problem. It is divided into four distinct scales, based on the frequencies at which the phenomena occur.

2.2 Applications

Before developing a model that can integrate the physical processes from the four levels mentioned in section 2.1, potential applications are identified from which relevant performance metrics and constraints are derived. The

performance metrics are used as variables to be modeled and the constraints are used as input.

[2] speculates on trends that are based on recent demonstrations with FSO satellite communication technology, shown in Table 2.1. Considering aircraft, the focus is expected to be on direct-to-user links and optical feeder links for LEO and medium-earth orbit (MEO) broadband constellations. In the case of optical feeder links, aircraft may function as gateways between space and optical ground stations (OGS) or direct end users on Earth. FSO direct-to-user applications can be divided into large-scale commercial services and defense services. The latter is likely to precede, as commercial services require exploitation on a large scale, which in turn requires a large number of multi-link satellites. The Space Development Agency (SDA) plans to operate the first constellation using optical uplinks and downlinks for defense purposes [25], making this a practical reference constellation.

Trends	Application
Broadband constellations	• ISL • Direct-to-user optical up/downlinks • Optical feeder links
Deep space communication	• ISL • Direct Earth-space • Relay
Short duration communication	• Imaging • Direct Earth-space • Sensing • Demonstrations
Geo-synchronous orbits	• Cyber security: QKD • Direct-to-user optical up/downlinks • Optical feeder links

Table 2.1: Current and future trends [2] of FSO communication services along with specific applications for each trend

In addition to the above trends, four drivers are defined that serve as the foundation for user requirements for FSO communication missions.

1. Capacity
   Capacity indicates the maximum achievable data transfer, or throughput, within a communication channel. Looking at Nielsen's Law, there is a large need for increasing capacity. The actual amount of throughput defines the overarching performance of a communication link.
2. Availability & Reliability
   Availability is an important metric for macro-scale mission performance [4], as it indicates the total available link time. This is typically expressed as a fraction of the total mission time. When zooming in onto micro-scale time scales, the reliability is characterized by the outages due to fluctuations of the laser. The degree of reliability is thus also an important metric for performance.
3. Latency
   Latency is a critical performance metric for all communication systems. Considering global satellite constellations that deal with large distances and routing between the satellites, latency becomes a very competitive metric [3] and thus a valuable metric to model. This is for now out of the scope of this study.
4. Security.
   Security benefits are an important market need for communications. This is also out of the scope of this study.

2.2.1 Performance metrics

From the defined mission drivers, the derived performance metrics are shown in Table 2.2. These are used as variables that the model will simulate. The metrics are as follows:

Aspects	Performance metrics	Model variables
Availability	Coverage	• AC trajectory • SC trajectories • Link selection
	Pointing	• Slew rates • Field-of-regard
Reliability	Link quality	• P_{RX} • BER • Fading statistics • FEC
Capacity	Throughput	• Data rate

Table 2.2: Performance metrics of the model

- Coverage
  Coverage is defined here as the probability that the satellites are within reach for communication with the aircraft, thus giving a good performance indication at mission level. Insight into the coverage can be obtained through the elevation of the satellites with respect to the aircraft, for which the relative states between these vehicles are required. For this, all trajectories need to be modeled, along with a link selection.
- Pointing
  The relative states between the aircraft and the satellites can also be used to simulate the slew rates and the field of regard (FOR). The first is defined as the relative angular rate of the satellite with respect to the aircraft or vice versa. The second is defined as the difference between the angle of the laser at the start and the end of communication. These variables are valuable metrics to simulate as they are typically design constraints of an LCT.
- Link quality
  The signal power at the receiving terminal P_{RX} is a commonly used metric, conveniently used with link budgets. This metric thus includes all gains and losses. BER indicates the probability of receiving erroneous bits and is thus an insightful metric regarding reliability. Statistics of signal outages can be used for sizing of the link reliability, making it a valuable metric to model. Interleaving and coding

schemes are typically used to improve performance [7, 27]. This improvement will be modeled as well.
- Throughput
  With capacity as a mission driver, the throughput gives a good indication of the mission performance. It is simulated as the total number of successfully transferred bits per second. Additionally, the total channel capacity can be estimated using the Shannon-Hartley theorem [28].

Next to requirements, the problem as described in section 2.1 also involves constraints. These are used as input parameters for the model. A division is made between hardware (LCT)-, environment- and mission constraints.

- Hardware constraints
  Mechanical, electrical and optical system characteristics of the transceiver terminals of both aircraft and spacecraft.
- Environment constraints
  The atmospheric properties are attenuation coefficient, background irradiance and cloud transmission.
- Mission constraints
  Initial conditions of the aircraft and constellation to use for the propagation of their trajectories.

2.2.2 Assumptions

Next to the input parameters, the model is also constrained by assumptions, shown in Table 2.3. The assumptions are discussed in more detail for each sub-model in chapter 3. Regarding the acquisition phase, a very large divergence is assumed with negligible pointing error. For uplinks and downlinks, the only assumed differences are the transmitter and receiver terminal properties and atmospheric turbulence effects, as explained in subsection 3.3.2.

2.3 Multi-Scale Method

2.3.1 Trade-off

For the integration and simulation of all physical processes from the four levels defined in section 2.1, a multi-scale method is used. In this section a proper multi-scale method is selected by trading off existing methods in Table 2.4. The criteria of speed and accuracy are used to ensure the efficiency of the method. Other criteria are versatility and complexity, as the aim of the model is for it to be used for the analysis of a real mission, as defined in section 2.1, and to be potentially extended to other missions. All metrics are given a weight, based on their importance for this specific problem. As the priority is a realistic model that can be implemented to multiple use cases, accuracy and versatility are given a weight of 2. Scores are based on the degree of fitness of the method with respect to each criterion, and are ordered as follows:

1. Red: No fit = 0 points
2. Orange: Low fit = 1 point
3. Yellow: Reasonable fit = 2 points
4. Green: Good fit = 3 points

Model level	Aspect	Assumption
Mission	Aircraft	• No airflow turbulence
	Routing	• Fixed acquisition time (50s) • Min. elevation (10°)
Link	LCT	• Bit-error-rate sensitivity is 1e-6 • One-mode fiber coupling • Power fraction reserved for ATS • Fixed path transmission
	Atmosphere	• Mie scattering • Static cloud loss
Channel	Turbulence	• Static turbulence spectrum (cut-off at 1000 Hz) • Hufnagel-Valley model for C_n^2 • Weak turbulence ($\sigma_I^2 << 1$) • Tip-tilt correction • Kolmogorov theory, rytov approximation
	Micro-vibrations	• Static mech. jitter spectrum (cut-off at 100 Hz)
	Beam propagation	• Spatial airy disk profile between lens and fiber • Spatial Gaussian profile between in channel
Bit	Coding	• Reed-Solomon scheme • Error spread is same as total bit spread
	Noise	• Dark current is neglected • Static background noise
	Modulation	• OOK-NRZ, M-PPM or BPSK
	Detection	• APD or PIN with preamp

Table 2.3: Assumptions for each level in the model

2.3.2 Assessed multi-scale methods

The TPCWM, proposed in [16], builds on a time-parallel (Parareal) approach [29], where a fine-scale response $\mathbf{y}_f$ and a coarse-scale response $\mathbf{y}_c$ are combined. This is done in parallel for each time step $\Delta\mathbf{T}_i$, where the fine response $\mathbf{y}^n_{f(i)}$ is used to iteratively correct the coarse response $\mathbf{y}^{n+1}_{c(i)}$. Combined (compound) wavelets are added to the method to efficiently combine the simulation of the coarse and fine response. However, a first-order similarity is required between $\mathbf{y}_f$ and $\mathbf{y}_c$, which can't be guaranteed, as turbulence and other micro-scale physics have a relatively large effect on the coarse solution problem. Hence, this method is not suitable for combining the processes of this specific problem. Nevertheless, the time-parallel approach is versatile and its notion can be used for the simulation of the micro-scale and macro-scale processes

The Coarse-grained Monte Carlo method (CGMCM), proposed in [30], uses a stochastic simulation framework, where Markov random fields are used to represent an undirected network of interdependent nodes through the

Table 2.4: Trade-off of all considered multi-scale methods, found in literature.

Criteria Weight	Computational Speed 1	Accuracy 2	Versatility 2	Complexity 1	Score
TPCWM	Parallel computation of micro/macro variables and wavelet method reduces computation cost	Micro-scale/macro-scale interaction occurs over the full-time interval	Assumes pre-existing overlap of micro/macro solution of 1^{st}order	Requires a combination of 2 methods: Time-parallel approach and CWM method	3×1 + 6×2 + 2×2 + 2×1 = 13
CGMCM	Allows for efficient coarse-graining of microscopic information by using cluster probability density function (PDF)s of multiple grids	Very efficient but at a computational cost compared to the analytically based CGMC method	Is almost exclusively used for Random Markov Field problems	Not all micro variables are random processes, thus requires combination with another method.	3×1 + 4×2 + 0×2 + 0×1 = 7
HMM	Original method uses a series approach (computation for each time step separately)	Micro-scale/macro-scale interaction occurs over the full-time interval	Applicable to a wide variety of problems	Intuitive method, but very generic. May become complex for certain problems	2×1 + 6×2 + 6×2 + 2×1 = 16
Sequential coupling	Number of dimensions is lower than number of dependent parameters	Only if efficient look-up tables and sufficient interpolation is used	Applicable to a wide variety of problems	Requires the use of look-up tables with 1 dimension for each dependent parameter	0×1 + 4×2 + 6×2 + 2×1 = 12

use of lattice grids. A Monte Carlo simulation is used for microscopic lattice grids, which are 'coarse-grained' to larger grids. While allowing many variables through the use of Monte Carlo, it greatly increases speed. However, this method uses an inherently stochastic approach with Markov random fields and is less suitable for the deterministic processes in our model. Adding deterministic variables requires an additional component to the method, increasing complexity. Hence, this method is not preferred for our specific problem.

The HMM, proposed in [15], uses a generic method to combine and simulate processes of various timescales. As a result, it can be intuitively applied to a wide variety of problems with relatively low complexity. This allows for any modifications of the model in case of extension to missions, such as GSL and ISL. The notion of this method is that a macroscopic state at time step n (U^n) uses microscopic information (D^n) from the microscopic state u^n in order to propagate to U^{n+1}. Complex multi-scale simulations have measured high accuracy, but relatively low numerical speed, due to the serial propagation. By combining the HMM with the TPCWM, a time parallel approach can be used instead of the serial approach, increasing efficiency.

The method of sequential coupling [31] implies a pre-computed microscopic state that is coupled to the macroscopic state. Microscopic information can be stored in look-up tables and mapped to the macroscopic state. This method differs from the others as coupling is not done concurrently but sequentially. Efficient use of look-up tables, suitable mapping and interpolation methods can lead to high accuracy. However, compared to concurrent coupling, it becomes too costly when $m > d$, where the missing information is a function of m macroscopic variables and the macroscopic state is simulated in d dimensions. For this specific problem, m is high, resulting in a costly micro-scale simulation.

2.3.3 Proposed method: MMM

Based on the trade-off, the HMM is the chosen multi-scale method. In order to further increase the speed of the serial propagation, the time-parallel approach from the TPCWM [16] is added to obtain a time-parallel HMM.

The proposed method is visualized in Figure 2.3. First, a relative state vector $\mathbf{G}$ is obtained by propagating all vehicles and choosing a link sequence. The first iteration of the macroscopic state $\mathbf{U}^{0,T}$ is simulated on mission level for all macro time steps $\mathbf{T}_i$, using $\mathbf{G}$ and hardware constraints $\mathbf{C}$. Then, for each $\mathbf{T}_i$, the microscopic state $\mathbf{u}_t^T$ is computed over all micro time steps $\mathbf{t}_j$, using the local macroscopic state and hardware constraints. $\mathbf{u}_t^T$ is then processed to obtain distributions in order to numerically compute convenient data such as fading statistics. Finally, the microscopic state is averaged and used for the iteration of the macroscopic state $\mathbf{U}^{1,T}$. The geometric output is directly computed with $\mathbf{G}$ and not iterated. The implementation of this method in our specified mission can be seen in Figure 2.4.

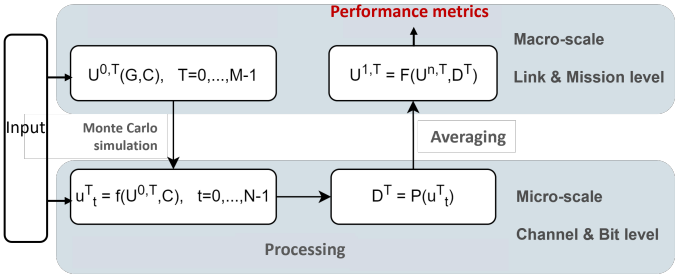

Figure 2.3: Graphical overview of the generic MMM

Multi-scaling requires a compromise between accuracy and efficiency. As microscopic information is converted to the macro-scale domain, time-specific information, such as temporal variations, will be lost. This gives rise to the question of which type of information is most relevant to

Type of output	Pro	Con
1 distribution of U^T over complete mission	Interpretable and full mission overview	Removing temporal information by making one distribution
Averaged time series of U^T	Better insight into specific links and elevation regions	Partly removing information by averaging
Time-specific link budgets	Interpretable and comparable to existing budgets	Partly removing information by averaging
Time-specific time series of u_t^T	Keep all micro information	Only applicable to specific macro time steps T

Table 2.5: Four defined types of output, based on the model drivers subsection 2.2.1

preserve and use as output. Four forms of output are identified in Table 2.5.

2.4 Model overview

The generic MMM, described in subsection 2.3.3, is implemented in an FSO communication mission between an aircraft and a satellite constellation, defined in section 2.1. Figure 2.4 shows this implementation as a high-level block diagram, where the blue blocks represent the time scales and the red lines represent the arrows of the MMM in Figure 2.3. The white blocks are the sub-models, that are further explained in this section. Considering modularity as one of the model drivers, all sub-models are aimed at being mutually exclusive and collectively exhaustive.

During this study, the focus was on the development of the end-to-end model. For this, we have attempted to realistically simulate the selected mission for a demonstration of the model. It should be noted that any input parameters can be tweaked in order to change the model output such that it better represents another mission.

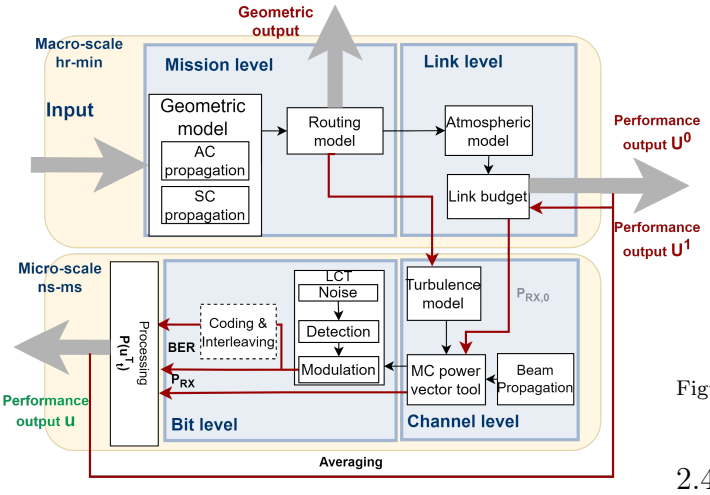

Figure 2.4: High-level block diagram of the MMM, applied to the defined mission

2.4.1 Macro-scale model

The macroscopic state $\mathbf{U}^T$ consists of a geometric component $\mathbf{U}_G^T$ and a performance component $\mathbf{U}_P^T$. The former consists of the aircraft state (position, velocity, height), satellite states (position, velocity, height) and relative states (range, elevation, azimuth, zenith, slew rate). The latter consists of the performance variable $P_{RX,0}$. The propagation models, along with the geometric model, compute $\mathbf{U}_G^T$. Then, the routing model selects a sequence of links and separates $\mathbf{U}_G^T$ for each link, where the link budget is computed for each time step $\mathbf{T}_i$. Macroscopic constraints are used in the micro-scale model that iterates $\mathbf{U}_P^{0,T}$ to obtain $\mathbf{U}_P^{1,T}$. The link budget is also iterated.

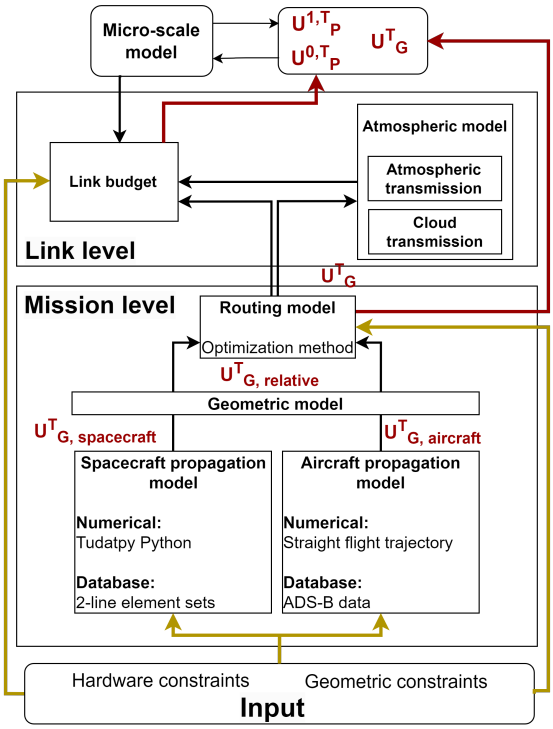

Figure 2.5: Block diagram of the macro-scale model

2.4.2 Micro-scale model

Following the multi-scale method, the microscopic state u_t^T is evaluated for each macro-scale time step $\mathbf{T}_i$. All simulated microscopic variables, depicted as green in Figure 2.6, are components of the microscopic state $\mathbf{u}_t^T$. Local macroscopic constraints are $P_{RX,0}$ and $\mathbf{U}_G^T$. Finally, $\mathbf{u}_t^T$ is processed to obtain a more convenient microscopic form $\mathbf{D}^T$ to convert to the macro-scale model. This processing includes a conversion of time series to distributions and numerical computation of fading statistics.

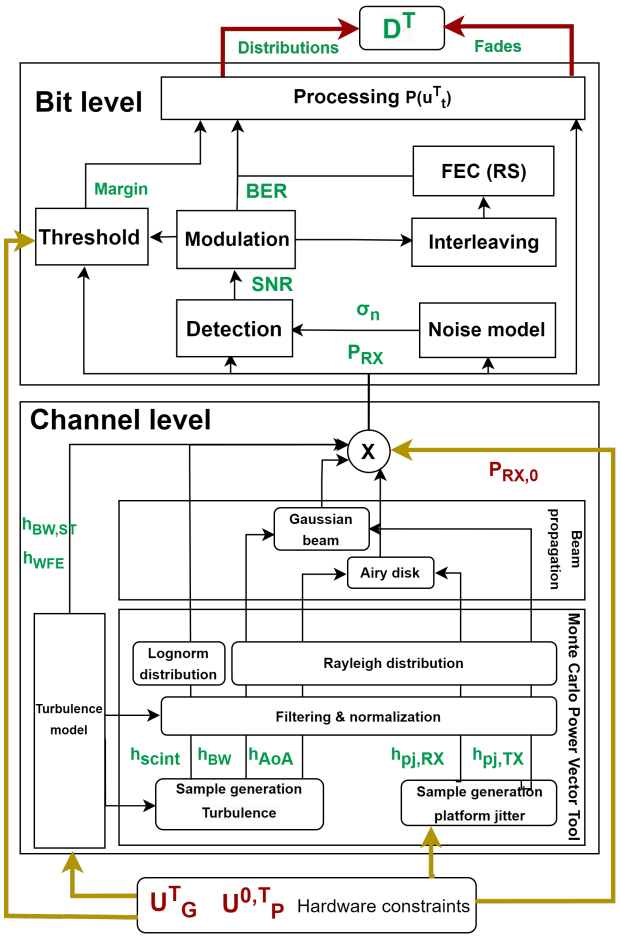

Figure 2.6: Block diagram of the micro-scale model

Chapter 3

Implementation

3.1 Mission level

3.1.1 SC propagation

This sub-model is used to obtain the geometric state vectors of the satellites $U^T_{G,SC}$. For the propagation of the satellites, astrodynamics propagation software Tudat is used, developed by Delft University of Technology [32, 33]. The propagation model set-up in Table 3.1 is chosen such that the propagation has a low computational cost, while still remaining accurate. Interpolation is performed such that the propagation time steps of 6 seconds match the macro-scale step sizes $\mathbf{\Delta T}$, in section 2.3. Propagation is performed in the Earth-Centered-Inertial (ECI) frame. See Appendix C for a more detailed discussion about the model selection and verification.

Keeping in mind modularity and versatility, the initial positions of the satellites can either be selected manually or extracted from real positional data. For the first, input parameters are the initial state (Cartesian or Keplerian elements), the number of planes and the number of satellites per plane. Assumed is that the planes and satellites are equidistant. Regarding the second, two-line element (TLE) sets [34] are retrieved from an open-source database Celestrak [35].

Table 3.1: Constellation propagation model set-up in Tudat.

Integrator	Runge-Kutta 4 (fixed step)
Step size	6 sec
Accelerations	• Earth point-gravity • J2 perturbation
Coordinate system	ECI
Interpolator	Linear

3.1.2 AC propagation

Here, the geometric state vector of the aircraft $U^T_{G,AC}$ is computed. The aircraft flight trajectory is obtained from an open-source database [36]. With the use of automatic dependent surveillance broadcast (ADS-B) data, this database provides state vectors of flight routes, which contain the speed, longitude, latitude, altitude and time. ADS-B data may contain hiatus due to a lack of connectivity of the aircraft during flight. Additionally, time steps provided by ADS-B are always 1 second, whereas the $\mathbf{\Delta T}$ might be different. Therefore, linear interpolation is performed. Raw data and linearly interpolated data are shown in Figure 3.1. The AC is propagated in the latitude, longitude, altitude (LLA) coordinate system. In order to obtain a valid relative geometric state between the satellites and the aircraft, the aircraft state is transformed to an ECI frame, described on pages 20-22 of [37].

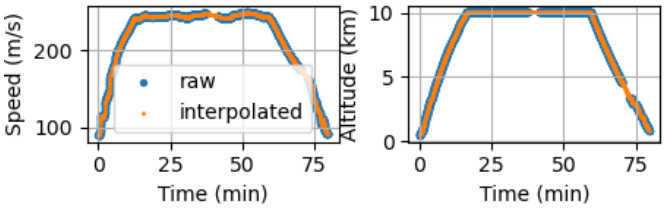

Figure 3.1: Aircraft trajectory for the flight route Oslo-Eneves. The data of the speed magnitude (left) and altitude (right) is directly extracted from [36].

3.1.3 Routing between AC and SC

With $U^T_{G,AC}$ and $U^T_{G,SC}$, the relative geometric state $U^T_{G,rel}$ is computed. This state contains the slant range, the looking angles (elevation, azimuth and zenith), the derived rates of these looking angles, and the slew rate. The latter is

defined as the rate of the angular speed of the satellite with respect to the aircraft.

Algorithm 1 Routing model

```
sats =< all satellite trajectories
t = 0
number of links = 0
acquisition time = 50
while t < end_t do
    sats_LOS = [ ]
    for sat in sats do
        if both conditions are met at t then
            add sat to sats_LOS
        end if
        choose sat with highest ϵ reach
        number of links += 1
        t += acquisition time
        start_time = t
        while condition 1 is met do
            t += 1
        end while
        add sats[current sat][start_t:t] to output
```

This sub-model performs a link selection between the aircraft and all propagated satellites. A simplified optimization method is developed, summarized in Algorithm 1. It optimizes the link time in combination with the highest elevation overpass. Two boundary conditions are used for every newly selected link:

1. The elevation angle between the satellite and the aircraft must be higher than 0°.

2. The elevation rate must be positive (rising satellite)

The minimum elevation angle is determined by the line-of-sight (LOS). In reality, this is slightly negative due to the altitude of the aircraft, but it is assumed zero for now. Having constrained the possible satellites available for linking up with, the satellite that reaches the highest elevation angle during one overpass is chosen, such to maximize both coverage and link time. It should be noted that this is a serial method and doesn't use a cost function. A more advanced optimization can be implemented for future purposes

3.2 Link level

3.2.1 LCT

As mentioned in subsection 2.2.1, there are constraints determined by the LCT system characteristics. Two sets of constraints are defined for both aircraft and spacecraft LCT, which are shown in Table 3.2. All parameter values are chosen based on industrial standards. Regarding the wavelength, 1.536 μm and 1.553 μm are used for the SDA constellation. The latter is used in this study.

Table 3.2: LCT system characteristics as defined in the model

LCT system aspect	parameter	Unit	AC	SC
Optics	Wavelength	nm	1553	1553
	Data rate	Gbps	2.5	2.5
	P_{TX}	W	20	10
	Aperture diameter	mm	80	80
	Clipping ratio	-	2	2
	Obscuration ratio	-	0	0
	beam width	mm	20	20
	Divergence (comm)	μrad	24.72	24.72
	Clipping loss	W	1.00	1.00
	Divergence (eff)	μrad	24.72	24.72
	Divergence (acq)	μrad	300	300
	M2 booster	-	1	1
	Focal length	cm	15	15
	Static pointing acc (std)	μrad	4	3.6
	Dyn. pointing acc (std)	μrad	3.4	3.3
	Field of View (comm)	ster	1e-8	1e-8
	Transmission loss	dB	-0.97	-0.97
	Static WFE loss	mm	100	100
	Splitting loss	-	0.9	0.9
Detection and Modulation	Optical bandwidth	GHz	2	2
	Electrical bandwidth	GHz	1	1
	Modulation scheme	-	OOK-NRZ	BPSK
	Detection scheme	-	Preamp. with PIN	Preamp. with PIN
	Amplification gain M	-	150	285
	Noise factor F		4	2
	Load resistor	Hz	50	50
	System temperature	K	300	300
	Quantum efficiency	-	0.8	0.8
Sensitivity	Threshold	BER	1.00E-06	1.00E-06
	Threshold	PPB	51.95	50.19
	Threshold	dBm	-43.0	-46.31
Coding	Symbol length	bits	8	8
	N, K	-	255, 223	255, 223
	Interleaving latency	ms	5	5

3.2.2 Link budget

The link budget is used to represent the integrated performance in terms of gains and losses, defined in Equation 3.1. TX and RX denote the transmitting and receiving terminal, respectively. The first iteration of the macroscopic state $U^{0,i}$ consists of the variable $P_{RX,0}$. By simulating the microscopic information with the use of MMM, $P_{RX,0}$ is updated with the microscopic losses h.

$$\begin{aligned} P_{RX} &= P_{RX,0}h \\ &= \left[P_{TX}G_{TX}\eta_{TX}h_{fs}h_{att}\eta_{RX}G_{RX}\right]\left[h_{p_{TX}}h_{p_{RX}}h_{scint}h_{outage}\right] \end{aligned} \tag{3.1}$$

where:

P_{RX} = Average TX optical power source
G_{TX} = Effective TX antenna power gain (Eq. 3.2)
η_{TX} = Internal TX path losses (Eq. 3.3)
h_{fs} = Free space loss
h_{atm} = Slow atmospheric loss (attenuation)
η_{TX} = Internal RX path losses (Eq. 3.3)
G_{TX} = Effective TX antenna gain (Eq. 3.2)
$h_{p_{TX}}$ = TX pointing loss (Eq. 3.6)
$h_{p_{RX}}$ = RX pointing loss (Eq. 3.7)
h_{turb} = Turbulence loss (Eq. 3.8)
h_{outage} = Additional power penalty

The diffraction gain G_{diff} is defined as the ratio of the far field power over the mean isotropic power, given a Gaussian beam profile [14]. Defocusing of the laser beam at the transmitter $T_{defocus}$ is commonly applied to size the divergence angle and thus affects the transmitter gain. Losses due to obscuration and clipping at the transmitter antenna are combined in $T_{clipping}$ and are directly related to the clipping and obscuration ratio [38]. For G_{RX} only G_{diff} is used.

$$G_{TX} = G_{diff} T_{clipping} T_{defocus} \tag{3.2}$$

The total system path loss of both terminals is defined in Equation 3.3. Splitting loss only applies to RX as the result of a reservation of a fraction of the signal for the Acquisition and Tracking System (ATS), where 10% is assumed. For coupling, a single-mode fiber is assumed, with a theoretical maximum efficiency of 81%. Finally, a system wave front error (WFE) of the laser of 100mm is assumed.

$$\eta = \eta_{coupling} T_{splitting} T_{WFE,static} \tag{3.3}$$
$$T_{WFE,static} = e^{2\pi WFE/\lambda} \tag{3.4}$$
$$\tag{3.5}$$

The micro-scale channel losses in Equation 3.1 are expressed by h. The pointing losses in Equation 3.6 and 3.7 include the effects of terminal platform jitter due to vibrations, and turbulence effects. Turbulence effects are beam wander and angle-of-arrival (AoA). All other turbulence losses are expressed by Equation 3.8 and include scintillation, WFE and beam spread, further explained in subsection 3.3.2. h_{outage} is added to take into account signal outages, further explained in subsection 3.5.3.

$$h_{p_{TX}} = h_{p_{TX,stat}} h_{p_{TX,dyn}} h_{BW} \tag{3.6}$$
$$h_{p_{RX}} = h_{p_{RX,stat}} h_{p_{RX,dyn}} h_{AoA} \tag{3.7}$$
$$h_{turb} = h_{scint} h_{WFE} h_{BS} \tag{3.8}$$

3.2.3 Atmospheric model

Atmospheric attenuation, caused by the scattering and absorption of molecules and aerosols, is treated as deterministic and is directly dependent on wavelength and geometric data. Considering slant range paths, the chosen sub-model uses Beer's law in Equation 3.9 with a varying attenuation coefficient ($\gamma(\lambda, z)$) that is based on the international standard atmosphere (ISA) model. It is described on page 6 of [39]. For the attenuation coefficient, a value of 0.0025 km^{-1} is assumed for molecular, Rayleigh scattering. It is also assumed that aerosol scattering approximately contributes the same, resulting in $\gamma(\lambda, 0)$=0.005 km^{-1}.

$$T_{att}(\lambda, z) = e^{-\int_0^L \gamma(\lambda,z) dz} \tag{3.9}$$

Only cirrus clouds are assumed for this mission, considering an aircraft altitude of 10 km. A static transmission of -0.96 dB is used, considering small effects above 10 km. It should be noted that even at these altitudes, complete outages are still possible in case of cloud blockage.

3.3 Channel model

3.3.1 Beam propagation

In the propagation channel, a Gaussian beam is assumed with beam waist w_0 defined by a fraction $1/e^2$ of the on-axis intensity I_0. in Figure 3.2a (left). At RX, after the light is received by the aperture, clipping of the telescope results in a reshaping of the beam, for which an Airy disk profile is assumed.

Pointing errors are divided into static and dynamic errors in Equation 3.6. The static errors are included in the link budget as static losses and losses due to dynamic errors are simulated with the tool described in subsection 3.3.3. The dynamic errors are expressed as power fluctuations by projecting the absolute misalignments over the beam profiles in Figure 3.2. For TX pointing errors θ_{TX}, projection is done over a normalized Gaussian off-axis intensity profile in Equation 3.11 and Figure 3.2a (right). As the receiving telescope diameter D_r is much smaller than the beam width at the receiver w_r, a point aperture is assumed at the receiver telescope, such that the power loss is equal to the intensity loss. The effective divergence angle in Equation 3.10 is computed by taking the diffraction-limited divergence angle $\theta_{div,DL}$, and adding clipping effects and defocusing effects. $M_{defocus}$ is the defocusing factor (set to 1 when turned off).

$$\theta_{div,eff} = \frac{\theta_{div,DL} M_{defocus}}{\sqrt{T_{clipping}}} \tag{3.10}$$

For RX pointing errors, between the lens and fiber coupling at RX, projection is done over a normalized off-axis power profile of an Airy disk in Figure 3.2b, which is obtained by integrating the intensity profile in Equation 3.12.

$$I/I_0 = \left(\frac{w_0}{w(z)}\right)^2 exp\left(-\frac{2\theta_{TX}^2}{\theta_{div}^2}\right) \tag{3.11}$$

$$I/I_0 = \left(\frac{J_1(k\frac{D_r}{2} sin(\theta_{RX}))}{k\frac{D_r}{2} sin(\theta_{RX})}\right)^2 \tag{3.12}$$

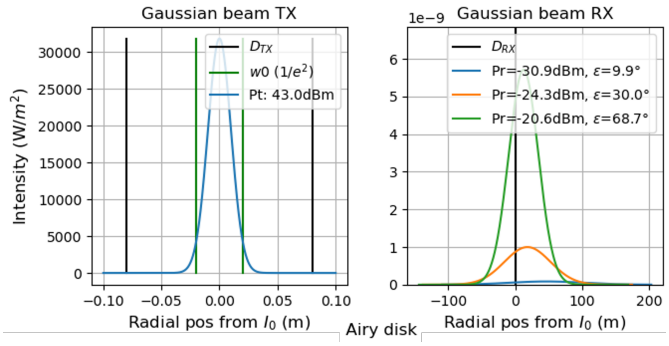

(a) Gaussian beam profile of the laser at the TX transmitter (left) and at the RX detector (right). (Right) shows three different macro-scale time steps T_i with the averaged pointing error at that time step, equal to $d_{TX} = \theta_{TX} L$.

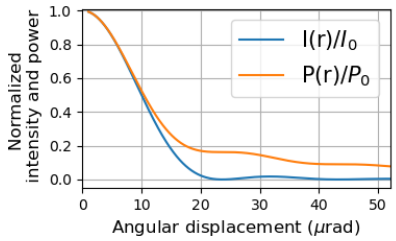

(b) Airy disk profile after RX detection

Figure 3.2: Optical beam profile of the normalized intensity as a function of the absolute radial displacement from the center-axis, due to pointing errors.

3.3.2 Turbulence model

Turbulence is modeled by simulating the strength of the signal power fluctuations and the temporal power spectrum. Kolgomorov theory is assumed, where the refractive index structure parameter C_n^2 is computed with the Hufnagel-Valley (HV) model [40], as it offers more generality through the inclusion of height variations and wind speed. Even though the HV model is an averaged approximation, it is currently the most realistic atmospheric turbulence and best-suitable for this mission. To compute the wind speed, a root mean square (RMS) of the Bufton wind speed model is used, described in Equation 3.13. For turbulence strength, only the right term is used, as this represents the real local atmospheric conditions. For the temporal power spectrum, the slew rate ω_{slew} and the aircraft speed V_{AC} are also included. Wind speed is only considered below 20 km, as turbulence can be neglected at higher altitudes [40]. As seen in Figure 2.6, all required geometric data for the HV model and the wind speed model is directly extracted from the geometric state U_G^T.

$$v_{rms} = \frac{1}{20 - h_{AC}} \int_{h_{AC}}^{20} \left[\omega_{slew} h + v_{AC} sin(\epsilon) + 30 e^{-\frac{h-9400}{4800}^2} \right] dh \tag{3.13}$$

For both uplink and downlink, Table 3.3 lists the assumptions made for each case. Beam spread, or short-term (ST) beam wander, and WFE are assumed to be slowly varying [8] [40] and expressed as mean normalized power terms. ST beam wander is derived on page 500 in [40]. Assuming a tilt-corrected beam, WFE in Kolgomorov turbulence can be computed through their low-order Zernike modes [41], from which a good estimate of the mean normalized intensity is obtained by equation 3 in [8].
The other effects are expressed as power fluctuations, for which the variances are computed using C_n^2, r_0 and geometric data. Uplink and downlink scintillation intensity variance is computed as described in [40]. Due to weak turbulence and small aperture size at RX, the aperture-averaging effect is only non-negligible below 10° elevation. The AoA variance approximation for uplink and downlink is described on page 491 in [40]. For uplinks, the long-term (LT) beam wander expression from page 502 in [40] is used. For downlinks, it is neglected, as beam wander only occurs at the end of the propagation path. Quantification of all simulated effects and variances for uplink and downlink, and for various elevation angles, can be seen in Table C.2 in Appendix C.
The assumed log-normal distribution for scintillation [1, 42] loses accuracy in moderate to strong turbulence regimes (σ_I^2>1). Considering aircraft platforms flying at altitudes well above the Earth's boundary layer (1-2 km), signal propagation is assumed to be in the weak turbulence regime. For all pointing jitter effects, a Rayleigh distribution is used [9].

3.3.3 Monte Carlo Power Vector Tool

This tool simulates all variables of the microscopic state u_t^T that are within the dedicated block of this tool in the block diagram in Figure 2.6. These variables are simulated as time series of power fluctuations, which occur in the time scale of 1 ms to 100 ms. They are combined into one power vector $h(t)$ and then multiplied with P_{RX_0} to obtain P_{RX}, as shown in Equation 3.14. The simulated variables are listed in Table 3.4. The tool is proposed in [7, 26]. Where the original method considers only beam wander and scintillation, this proposed extension adds 3 other jitter effects.

Table 3.4: Spatial fluctuation sources for the Monte Carlo simulation

Source	Fluctuation	Unit	Distribution
Turbulence	Scintillation h_{scint}	Norm. power (P/P_0)	Lognormal
	Beam wander θ_{BW}	Angle (rad)	Rayleigh
	AoA θ_{AoA}	Angle (rad)	Rayleigh
Platform	Jitter (TX) $\theta_{pj,TX}$	Angle (rad)	Rayleigh
	Jitter (RX) $\theta_{pj,RX}$	Angle (rad)	Rayleigh

$$h(t) = h_{scint} h_{TX}(\theta_{pj,TX}, \theta_{BW}) h_{RX}(\theta_{pj,RX}, \theta_{AoA}) \tag{3.14}$$

The steps for generating the power fluctuations are shown in Figure 3.3, where the micro-scale time series of each effect is simulated with a population of M samples. The temporal behaviour of each effect is simulated by (1) sampling from a standard normal distribution (top of 3.3), after which (2) normalizing and filtering is performed by applying a fast-Fourier transform (FFT) and using a Butterworth filter of order 2 in the frequency domain (2nd top

Table 3.3: Turbulence effects for uplink and downlink

Effect	Downlink	Uplink	Description	Static/Dynamic
Scintillation	Yes (plane wave) [40]	Yes (spherical wave) [40]	Intensity fluctuations	Dynamic
Beam wander ST	No (neglible)	Yes [26]	Spatial spread, seen from TX	Static
Beam wander LT	No (neglible)	Yes [40]	Angular displacement, seen from TX	Dynamic
AoA	Yes (several μrad) [40]	Yes (Sub μrad) [40]	Angular displacement, seen from RX	Dynamic
WFE	Yes [8]	Yes [8]	Phase fluctuations	Static

of 3.3). This process generates a temporal power spectrum for both turbulence and platform jitter effects.

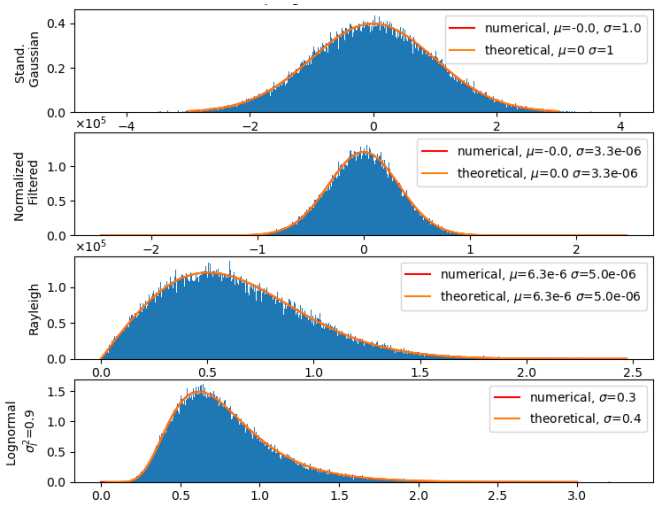

Figure 3.3: The 3 generation steps of the distributions. The bottom 2 plots are the same step, but for a different effect (jitter in top plot, scintillation in bottom plot)

The cut-off frequency of the power fluctuations due to turbulence is computed as in Equation 3.15, as described on page 366 of [40]. v_{rms} is the RMS of the transverse wind speed, perpendicular to the transmitted or received beam, for which all terms of the wind model are used in Equation 3.13 [43]. d is the speckle size at the receiving aperture. During the Kirari's Optical Downlink to Oberpfaffenhofen (KIODO) demonstration, a scintillation frequency of 120 Hz is typically measured with a wavelength of 808 nm and with an optical ground station [7, 44]. A larger wavelength of 1550 nm results in lower frequencies, but the large wind speeds increase the frequency up to 350 Hz.

$$\omega_t = v_{rms}/d = v_{rms}/\sqrt{\frac{L}{k}} = v_{rms}/\sqrt{\frac{H\lambda}{2\pi cos(\epsilon)}} \quad (3.15)$$

The platform jitter cut-off frequency depends on the ability of the LCT tracking system to correct for micro-vibrations of the platform and tracking noise. The temporal power spectrum is based on the measured power spectral density (PSD) of the Zephyr LCT, developed by Airbus [45]. For sufficient resolution, a sampling frequency of 10.0 kHz (0.1 milliseconds) is used. Figure 3.4 shows the frequency spectra of beam wander and platform jitter at TX (left) and the combined effects (right) at an elevation angle of 10°, where the cut-off frequency is 51.0 Hz. The spectra show that turbulence is dominant in the low-frequency regime and the platform jitter in the high-frequency regime.

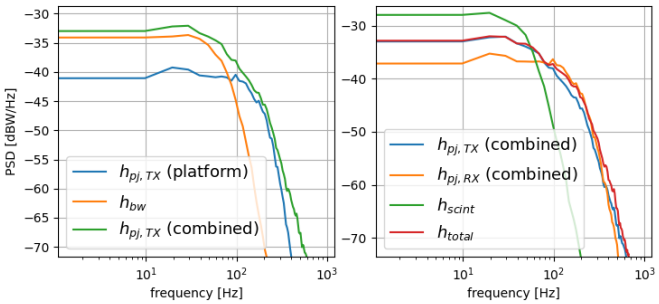

Figure 3.4: Simulated power spectral density of TX fluctuations (left) and combined fluctuation terms of h_{TX}, h_{RX}, h_{scint} and h (right)

Spatial variations are then introduced by converting the normalized distributions to the ones defined in Table 3.4 (2 bottom plots of 3.3). The x- and y-components of the angular deviations are assumed to be statistically independent and are sampled separately after which a root sum square (RSS) is taken to obtain the radial component. The histograms of all distributions can be seen in Figure 3.5, where the jitter losses h_{TX} and h_{RX} are described by a beta distribution [46].

As seen in Equation 3.14 the process includes a summation of distributions θ_{BW}, $\theta_{pj,TX}$ and θ_{AoA}, $\theta_{pj,RX}$, and a product of distributions h_{scint}, h_{TX} and h_{RX} for which it is approximated that all distributions are statistically independent. This is the case for the summations, but not for the product, as the turbulence effects are correlated. However, the verified outcome shows reasonable agreement with this assumption. See Appendix C for the detailed verification steps.

Figure 3.5: Histogram of all microscopic losses and their combined loss (top), and the resulting P_{RX}, at an elevation angle of 10°

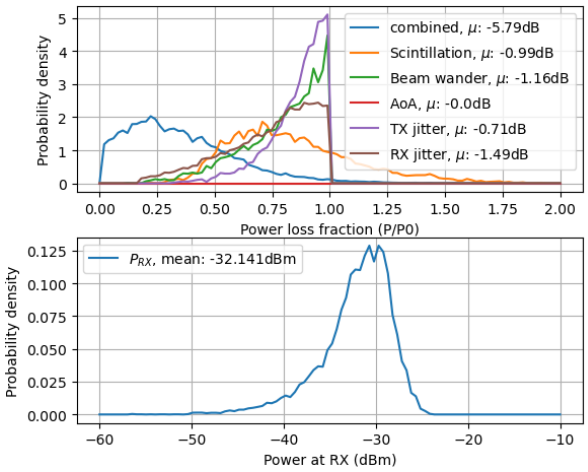

3.4 Bit level

As all processes at this level are computed with analytical equations, the time scale that is used here is the same as that in the channel level (1 ms to 500 ms). We thus assume here that for each time step all bit processes are identical. A sequence of processes is considered at this level, starting with (1) the reception the signal, including noise, then (2) converting the optical signal to an electric signal, then (3) (de)modulating between the electrical signal and discrete bits and finally (4) (de)interleaving and FEC.

3.4.1 Noise

This sub-model in Figure 2.6 computes the microscopic variable of noise power σ_n. Four noise contributions are considered significant regarding an optical signal: signal-dependent shot noise, background noise, thermal noise and noise-against-noise beating. Analytical expressions are used as shown in Table 3.5, assuming a Gaussian distribution for all contributions. In the case of shot noise, this assumption holds for large numbers of photo-electrons above 10-20 photons per bit [28], which is lower than the defined threshold in Table 3.2.

Table 3.5: Noise contributions with their expressions

Contribution	Analytical expression	Ref.
Shot noise σ_{sh}	$4S_N P B_E$	[47]
Beat noise σ_{beat}	$2mR^2 S_N^2 \left(B_o - \frac{B_E}{2}\right) B_E$	[47]
Background noise σ_{bg}	$L(\lambda) A_{RX} \Omega \Delta\lambda$	[48]
Thermal noise σ_{th}	$\frac{4kT_E}{R_L} B_E$	[28]

Due to the square-law response, where a photo-detector outputs an electric signal proportional to the square of the optical input signal, two optical fields are detected as shown in Equation 3.16. Shot noise can be interpreted as the cross-term $2AN$ of this response and the noise-against-noise beating is interpreted as the N^2 term [47]. The single-sided power spectral density S_N is described on page 84 of [47] and includes potential excess noise and gain in case of an amplified signal. B_o is assumed twice the B_e and 0.8 times the data rate, considering industrial standards.

$$P(t) \approx (A+N)^2 = A^2 + 2AN + N^2 \tag{3.16}$$

Considering a very small background radiation effect, a simplified expression is used as a worst-case scenario with direct sunlight, where the solar irradiance $L(\lambda)$ is based on the exo-atmospheric spectrum at 1 AU, equaling a value of 0.5 W/cm^2/nm/ster for 1550 nm wavelength.

3.4.2 Detection and Modulation

During detection and modulation, the SNR and the BER are simulated as two variables of the microscopic state u_t^T in Figure 2.6. To increase the versatility of the model, multiple detection and modulation schemes are implemented, as shown in Table 3.6. Only direct-detection (DD) techniques are considered, including Avalanche Photo-Diode (APD) detection and PIN detection, with and without an optical pre-amplifier. Unamplified-PIN schemes are typically limited by thermal noise and amplified-PIN and APD schemes are limited shot noise due to signal amplification [47], which is verified for this model. The most commonly used modulation schemes On-Off keying (OOK), Binary phase-shift keying (BPSK) and M-ary Pulse position modeling (PPM), are implemented.

All system characteristics considering detection and modulation are also shown in Table 3.2. Detection schemes are parameterized as direct analytical relations between the Quality factor (Q), the noise and P_{RX} [47]. Q is expressed as in Equation 3.17, where i is the electric current and σ is the noise. Modulation schemes are parameterized as analytical relations between Q and BER. See Table 3.6 for an overview of these expressions. A BER threshold of 1.0e-6 is assumed. The sensitivity is defined as the minimum P_{RX} to achieve a required BER threshold. This is determined by reversing the relations of Table 3.6.

$$Q = \frac{i_1 - i_0}{\sigma_1 - \sigma_0} \tag{3.17}$$

From a simulation of fluctuating BER values, the average BER is obtained by integrating the BER over the probability density function of the fading channel [49] [50].

3.4.3 Coding

The coding sub-model in Figure 2.6 updates the BER variable by including extra performance due to interleaving and FEC coding. One of the most commonly used FEC coding schemes is Reed Solomon (RS) [51], which is used in this research in combination with a (de)interleaving scheme. Assuming a (255,223) RS coding scheme, an 8-bit symbol size, a 2.5 Gbps data rate and a 5 sec (50k) microscopic population size, there are $2.5 * 5/223 * 8 = 7.0e6$ code words. Due to high computational cost, the FEC performance is analytically approximated based on the Voyager mission [27, 51], shown in Figure 3.6.

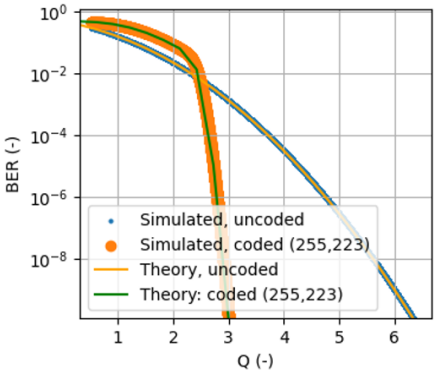

Figure 3.6: Analytical approximation of Reed Solomon (255,223) FEC coding performance, compared to the uncoded channel BER. Theoretical model by [27]

RS coding results in increasing performance only beneath BER≈1e-3, due to corrupted code words at higher BER

Table 3.6: Detection and (de)modulation techniques with their expressions.

Detection			Modulation		
Scheme	Q	Ref.	Scheme	BER	Ref.
PIN	$\frac{PR}{2\sigma_{th}}$	[28]	OOK-NRZ	$\frac{1}{2}erfc(\frac{Q}{2})$	[28]
PIN (amplified)	$\frac{G_o}{\sigma_{sh}+2(\sigma_{bg}+\sigma_{beat}+\sigma_{th})}$	[47]	BPSK	$\frac{1}{2}erfc(Q)$	[28]
APD	$\frac{G_e}{\sigma_{sh}+2(\sigma_{bg}+\sigma_{beat}+\sigma_{th})}$	[47]	M-PPM	$\frac{M}{4}erfc\left(\frac{1}{2}Q^2\sqrt{Mlog2(M)}\right)$	[28]

[27]. Therefore, interleaving is typically used in addition. An interleaving latency of 500 ms is used, as the interleaver should have a length of around 20 times the coherence length [14], which is assumed as the lowest simulated turbulence frequency (around 40 Hz). The interleaver is implemented in the model by spreading out the BER values of each sample over N microscopic samples in Equation 3.18.

$$N = 500/\delta_t = 500/0.1 = 5000 \tag{3.18}$$

3.5 Data processing

Looking at the MMM in Figure 2.3, processing is performed on the microscopic state u_t^T, which happens on bit level in the model overview in Figure 2.4. Processing is done in order to obtain the throughput and the fading statistics. Then, the fading statistics are expressed as a loss (the power penalty), such that they can be accounted in the link budget as h_{outage}.

3.5.1 Throughput

Firstly, the channel capacity is computed with the Shannon-Hartley expression, as described on page 111 of [28] and shown in Equation 3.19. The capacity is computed for each macro-scale time step with the bandwidth filter B as defined in Table 3.2 and an averaged SNR that includes the power penalty, described in Equation 3.21.

$$C = Blog_2(1 + SNR) \tag{3.19}$$

The actual throughput is computed by estimating the total number of successfully received bits, as in Equation 3.20. Here, DR is the data rate and Δt is macro-scale time step. A required minimum outage probability of 1% is used, any larger outage fractions on micro level are assumed to result in zero throughput on macro level.

$$T = DR\Delta t(1 - BER) \tag{3.20}$$

3.5.2 Fading statistics

Fades in the received signal provide information regarding the outage probability and time-specific fade lengths. Fading statistics include fade time (mean), the number of fades and fractional fade time (outage probability). The statistics are numerically computed and are solely based on P_{RX} and the terminal sensitivity (expressed as the threshold signal power $P_{RX,thres}$), which is shown in the pseudo-code in algo. 2. The computations are derived from the analytical expressions from [40].

Algorithm 2 Fade statistics

```
N =< macro-scale time steps
M =< micro-scale population size
t_Δ <= 5 sec
t_δ <= 0.1 ms
frac fade time =< count nonzero(P_RX < P_thres)/M)
number of fades = 0
for T = 1, 2, ..., N do
    for t = 1, 2, ..., M do
        if P_RX[T, t] < P_thres & P_RX[T, t−1] > P_thres then
            number of fades += 1
            mean fade time <= frac fade time / number of fades * (t_δ * M)
```

3.5.3 Power penalty

When averaging P_{RX} from micro-scale to its macro-scale variant, all information regarding fades is lost. In order to keep this information, an additional power penalty h_{outage} is added, as defined in Equation 3.21. The numerical computation of this loss is derived from the analytical method proposed by [52]. However, instead of only accounting for scintillation in [52], the method is extended to the combined signal P_{RX} with all micro-scale fluctuations defined in subsection 3.3.3. P_{min} in Equation 3.21 is obtained by setting a required outage probability, where P_{min} is the minimum average power that is needed to maintain this outage probability (set to 1% in this study). The numerical computation is shown in the pseudo-code in algo. 3.

$$h_{outage} = \frac{P_{min}}{P_{RX,avg}} \tag{3.21}$$

Algorithm 3 Power penalty

```
required outage = 0.01
diff = inf
for P in P_range do
    outage =< count nonzero(P_RX < P)/M)
    diff1 = abs(outage - required outage)
    if diff1 > diff then
        diff1 =< diff
        P_min =< P
```

3.6 Verification and Validation strategy

The V-model consensus is applied for verification and validation of the model. The numerical model is divided into three levels, as shown in Figure 3.7: Single code functions, sub-models and the integrated model. This study has performed (1) verification at sub-model level, (2) convergence analysis of the full model and (3) a full model demonstration with respect to a defined use case.

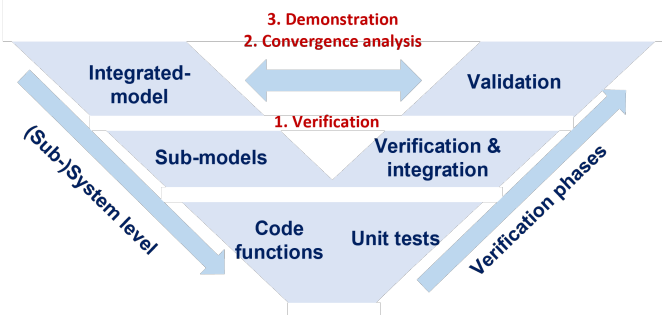

Figure 3.7: Verification & validation steps in the V-model

3.6.1 Verification

The sub-models are extracted from literature and some are modified wherever necessary, as explained for each sub-model in 3.1 to section 3.5. Verification is performed by successfully replicating the methods from literature with dummy data, if possible. Additionally, numerical and visual accuracy tests are performed for each sub-model, after which they are integrated and successfully verified again. A more detailed verification strategy, along with an elaboration on the results, are found in Appendix C.

3.6.2 Convergence analysis

Convergence analysis is performed with two model parameters: (1) the macro-scale step size ΔT and (2) the micro-scale population size M. These are selected based on a prioritization of all model parameters. Stochastic uncertainty and sensitivity are used as the two criteria for this prioritization, because a combination of these are considered to be critical for the model.
Additionally, a sensitivity analysis is performed for three input parameters: (1) The transmitter aperture size D_t, (2) the turbulence cut-off frequency f_c and (3) the flight route. For the first two, 4 different values are chosen. For the last one, two routes are chosen that differ in coverage, such that their performance is different. Coverage is defined here as the range of elevation between aircraft and satellites. Table 3.7 shows the selected parameters and their ranges. Regarding the performance metrics, the outage probability and mean fade time are an important measure for the convergence of the signal reliability and the signal variance is a measure for the convergence of the total signal. A threshold of 0.5 dB is used for signal variance and 5% for the fading statistics. The analysis is performed by simulating the model over the defined range of the model parameters, for each combination of input parameters, resulting in a total of 1200 runs.

The analysis shows that signal variance behaves similarly in all cases, converging rapidly. However, convergence of the outage probability and mean fade time is worse for the high-coverage case. This can be explained by weaker turbulence at a higher elevation regime, which results in insufficient fade samples for reliable statistics. As divergence starts only at an outage probability lower than 0.1%, this is not considered as a problem. The largest possible ΔT at which the model still converges is 6 seconds. The smallest possible micro-scale M is 5 seconds. Furthermore, f_c only affects the mean fade time, but doesn't impact convergence. D_t has a large impact on the mean signal power and the model doesn't converge for D_t higher than 8 cm for high coverage and 5 cm for low coverage. The convergence analysis is discussed in more detail in Appendix C section C.5.

Table 3.7: Selection of all parameters for the convergence analysis

	Parameter	Values
Model	Step size ΔT (s)	1.0,...,10.0 (steps of 0.5)
	Population size M (s)	0.1,...,10.0 (steps of 0.5)
Input	Flight route	Oslo-Eneves Sydney-Melbourne
	Aperture D_t (cm)	2.0, 5.0, 8.0, 10.0
	Cut-off frequency f_c (ms)	0.5, 0.75, 1.0, 1.5
Metrics	Outage probability (%)	5.0
	Mean fade time (%)	5.0
	Signal power (dB)	0.5

3.6.3 Demonstration

Finally, the test case with the Oslo-Eneves flight route is chosen for the demonstration, as this case includes a larger range of performance due to its widely varying elevation. This test case is simulated and its results are analyzed and compared to similar studies in literature in chapter 4.

Chapter 4

Results and Discussion

4.1 Geometry

As described in section 3.6, two test cases are chosen for the convergence analysis:

1. The high-coverage route Oslo-Eneves (59.9°N->68.46°N, 10.7°E->16.7°E)
2. The low-coverage route Sydney-Melbourne (37.81°S->33.87°S, 151.21°E->144.96°E)

The distribution of the elevation angles and slew rates are visualized for each link in Figure 4.1b as the performance metrics regarding coverage and pointing, as described in subsection 2.2.1. It shows an elevation range of 0° to 70° for case 1 and 0° to 20° for case 2. Furthermore, higher elevation angles correspond to higher slew rates up to a maximum of 0.34 °/s at 70 ° elevation, which agrees with the theoretical expression of Equation 4.1

$$\Omega_{max} = V_{orbit}/\Delta h = 2\pi \sqrt{\frac{(R_{earth} + h_{sc})^3}{\mu_{earth}}}/(h_{sc} - h_{ac}) \tag{4.1}$$

Looking at Figure 4.1a, we see that the Oslo-Eneves (blue line) route is within reach of both planes, unlike Sydney-Melbourne (orange line) that only links with one plane. Oslo-Eneves also has a higher average link time than Sydney-Melbourne (12.3 min versus 8.0 min), which is expected due to the higher coverage of the first. Finally, a more or less constant increase is observed in the maximum elevation reach for each link, visible in the Figure 4.1b by the curve peaks moving towards the right. This can be explained by the rotation of the earth, causing a constant rotation of the aircraft with respect to the satellite constellation.

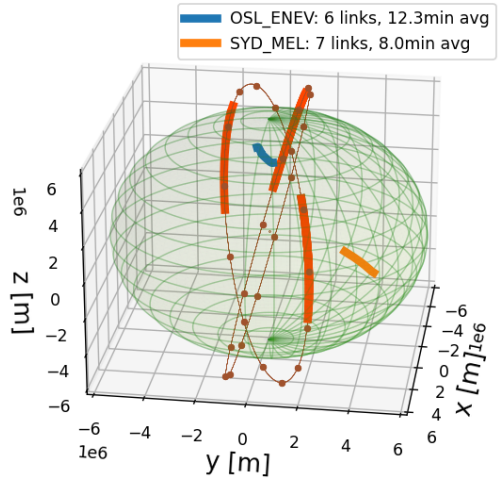

(a) AC trajectories (blue and light orange), satellite orbits (brown) and links (red)

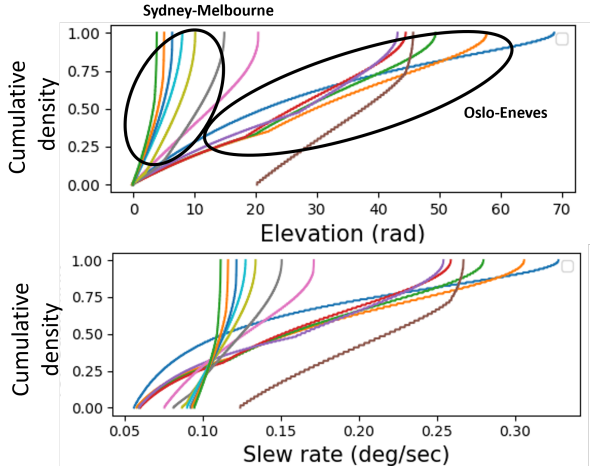

(b) Coverage and slew rate CDF

Figure 4.1: Macro-scale geometric state U_G^T of both test cases

4.2 Performance

A full demonstration is performed for case 1, as this case includes a larger range of elevation angles, as seen in Figure 4.1b. The output of the end-to-end model with this demonstration contains the performance metrics defined in subsection 2.2.1, in the forms defined in Table 2.5.

4.2.1 Macro-scale

Figure 4.2 shows distributions of BER and P_{RX} that consist of all microscopic samples throughout the full mission, thus without averaging. An outage probability of 8.0% is computed for P_{RX} and 8.2% for BER. Theoretically, the outage probability for P_{RX} and BER should be the same here, as the power threshold $P_{RX,thres}$ is derived from the BER threshold BER_{thres} by numerical inverting the analytical expressions that compute BER from P_{RX} in Table 3.6. The error is thus likely introduced in this numerical inversion. These distributions give a fair preliminary insight at high level. However, this comes at the cost of temporal information. Hence, Table 2.5 suggests output types that include more information, such as time series and link budgets.

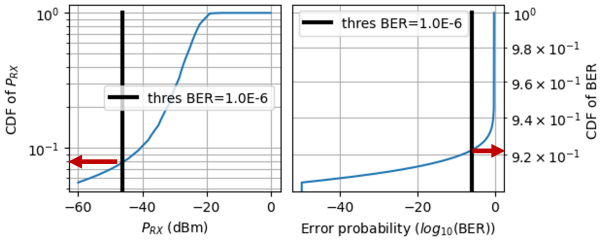

Figure 4.2: CDF of P_{RX} and BER over the complete mission, including all links

Each curve in the time series output of Figure 4.3 represents a separate link, where the differences in performance are explained by different altitudes and wind speeds during the climb and descent of the aircraft in Figure 3.1, resulting in differences in turbulence. $P_{RX,0}$ (yellow line) represents the macroscopic state $\mathbf{U}^{0,T}$ and $P_{RX,1mean}$ (blue line) represents $\mathbf{U}^{1,T}$, averaged. When adding the power penalty h_{outage} the difference between $\mathbf{U}^{0,T}$ and $\mathbf{U}^{1,T}$ increases to -10 dB at high elevation to -80 dB at low elevation, confirming the relevance of microscopic information in the model. The difference is larger at low elevations due to the exponential relationship between turbulence strength and the power penalty [52]. Furthermore, using a 2.5 Gbps data rate, the to-

tal throughput modeled over the complete mission is 9.2 TB, out of a maximum of 13.5 TB over the total mission interval. Using the Shannon-Hartley theorem, the maximum achievable data rate is much higher, indicating the relevance of variable data rate techniques. Complete communication outage (no throughput) occurs when P_{RX} is below the threshold (green line in Figure 4.3), which corresponds to the assumption of communication outage below 1% outage probability. With increasing elevation, the BER decreases, resulting in an increase of the throughput, as expected in Equation 3.20. The BER plotted in Figure 4.3 is without coding. When applying coding, error-free communication is achieved above 5°-10° elevation (BER = 1e-50), depending on the link.

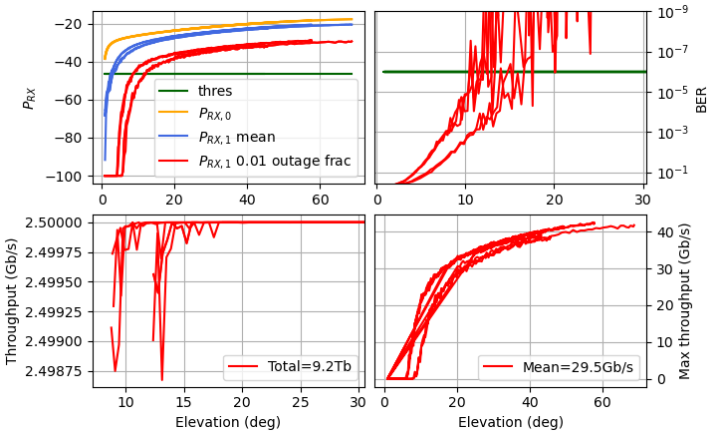

Figure 4.3: Averaged P_{RX} (upper left), BER (upper right), throughput (lower left) and channel capacity (lower right) at macro-scale level

Link budgets are simulated for each macro-scale time step ΔT, of which one is extracted at an elevation angle of 10° in Table 4.1, for both uplink and downlink, and communication and acquisition. As discussed in chapter 3, system losses are treated as static losses, geometric losses, attenuation, ST beam wander and WFE are treated as deterministic macro-scale losses. The attenuation loss is relatively high considering the high altitudes of the aircraft, due to 0.97dB cloud loss on top of the 0.42dB attenuation loss.

For the micro-scale losses, ensemble averages are taken from the microscopic variables, with the additional penalty h_{outage} that accounts for the required outage probability. For uplinks, the jitter at TX is dominant (-2.7 dB) and all micro-scale losses add up to -4.9 dB with a penalty of -11.2 dB. For downlinks, jitter at RX is dominant (-2.0 dB) and all micro-scale losses add up to -3.2 dB with a penalty of -8.3 dB. The difference in losses is explained, firstly by the fact that uplink beam wander fluctuations are stronger than downlink AoA fluctuations. Secondly, scintillation for uplinks is more severe due to turbulence occurring close to the receiver. Furthermore, the large power penalties indicate the relevance of the fading statistics with respect to mission performance.

The acquisition budget differs from the communication budget through the much larger divergence angle of 300μrad. This results in a much lower antenna gain and thus a lower P_{RX}. However, as the pointing errors are assumed negligible, the only micro-scale loss is caused by scintillation. The power penalty is neglected here, as the sensitivity during acquisition is very high compared to the sensitivity during communication.

Table 4.1: Link budget of uplink and downlink at 20° elevation

Term	Unit	Uplink		Downlink	
		Comm	Acq.	Comm	Acq.
TX					
P_{TX}	dBm	43.0	43.01	43.02	43.02
λ	nm	1553.0	1553.0	1553.0	1553.0
Data rate	Gb/s	2.5	0.0	2.5	0.0
$\theta_{div,diff}$	urad	24.7	24.72	24.72	24.72
$\theta_{div,eff}$	urad	25.7	300.0	25.73	300.01
ϵ_{pe}	urad	4.0	0.00	3.60	0.00
σ_{pe}	urad	3.4	0.00	3.30	0.00
G_{TX}	dB	101.17	79.5	101.17	79.49
$T_{coupling}$	dB	-1.0	-1.0	-1.0	-1.0
$T_{WFE,static}$	dB	-0.7	-0.7	-0.71	-0.71
$T_{pe,static}$	dB	-0.2	-0.2	-0.17	-0.17
RX					
Aperture	mm	80.0	80.0	80.0	80.0
$\epsilon_{pe,RX}$	urad	3.6	0.00	4.00	0.00
$\sigma_{pe,TX}$	urad	3.3	0.00	3.40	0.00
G_{RX}	dB	104.18	104.2	104.2	104.2
$T_{coupling}$	dB	-1.0	-1.0	-1.0	-1.0
$T_{WFE,static}$	dB	-0.7	-0.7	-0.7	-0.7
$T_{splitting}$	dB	-0.5	-0.3	-0.46	-0.35
$T_{pe,static}$	dB	-0.4	-0.4	-0.46	-0.46
Free space					
Range	km	3102.6	3102.6	3102.6	3102.6
Elevation	deg	10.1	10.1	10.1	10.1
T_{fs}	dB	-268.0	-268.0	-268.0	-268.0
Channel (macro)					
T_{att}	dB	-1.78	-1.78	-1.78	-1.78
$T_{BW,ST}$	dB	-0.001	-0.001	-0.0	-0.0
T_{WFE}	dB	-0.04	-0.04	-0.04	-0.04
Channel (micro)					
h_{TX} jitter	dB	-2.7	0.00	-0.6	0.00
h_{RX} jitter	dB	-1.3	0.00	-2.0	0.00
h_{scint} los	dB	-0.9	-0.9	-0.6	0.6
$h_{penalty}$ (1%)	dB	-11.2	0.00	-8.3	0.00
RX signal					
$P_{RX,0}$ (static)	dBm	-26.2	-47.0	-26.3	-47.0
P_{RX} (dynamic)	dBm	-42.7	-47.9	-37.6	-47.6
Tracking P_{RX}	dBm	-52.2	-56.5	-47.1	-56.5
Foot sprint	m	76.7	930.8	76.7	930.8
Link margin					
Threshold (1.0e-6)	BER	1.0e-6		1.0e-6	
	PPB	73.1		156.7	
	dBm	-46.3		-43.0	
Threshold tracking	dBm	-65.0	-65.00	-65.00	-65.00
Link margin	dB	3.6		5.4	
Link margin tracking	dB	12.8	8.2	17.8	8.5

4.2.2 Micro-scale

Figure 4.4 shows the micro-scale time series of P_{RX} and BER at three macro-scale time steps ΔT: At 10°, 30° and 69°. The behaviour of P_{RX} and BER are consistent, looking at the corresponding minima of the blue curve at 1361 ms, 1374 ms and 1434 ms. The observed high P_{RX} margins correspond to very low BER values. A minimum BER of 1e-50 is used. Looking at the temporal behaviour, an increase in elevation causes an increase in frequency. This can be explained by the fact that the cut-off frequency of turbulence increases with increasing elevation, due to the higher transverse wind speeds (Equation 3.15).

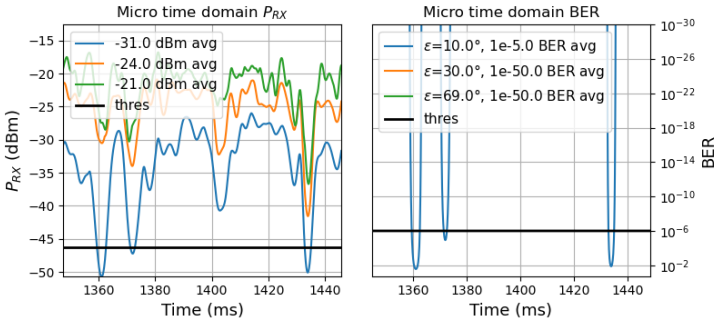

Figure 4.4: Micro-scale evaluation of P_{RX} and BER at 10° elevation

As explained in subsection 3.3.3, the spectra of both turbulence and platform jitter are flat, resulting in a flat spectrum of P_{RX} in Figure 4.5 (right). Again, three macro-scale time stepΔT, at 10°, 30° and 69° are plotted. The total area of the PSDs decreases with decreasing elevation. This is expected as lower elevation results in a lower P_{RX}, which is equal to the area beneath the curve. Furthermore, despite the varying turbulence cut-off frequency, all spectra seem to stop around 100 Hz, which is equal to the cut-off frequency of the platform jitter. The auto-correlation function of P_{RX} at 10° elevation in Figure 4.5 (left) indeed reveals covariance between $P_{RX}(t)$ and $P_{RX}(t+\tau)$ for τ up to 10 ms (100 Hz), indicating that the platform jitter frequency dominates the temporal behaviour. However, for higher elevation angles of 30° and 69°, covariance decreases to around 3 ms to 5 ms, indicating a more dominant turbulence frequency, likely due to the large transverse wind speeds in this elevation regime.

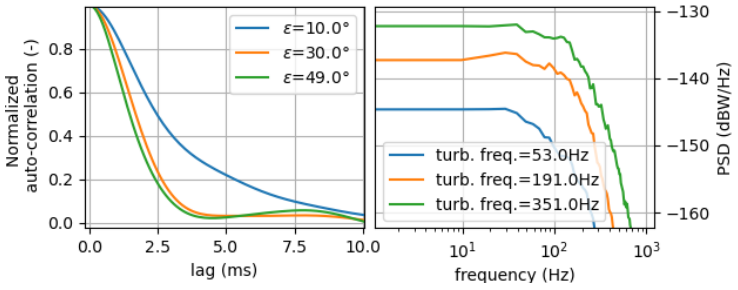

Figure 4.5: Normalized auto-correlation function (left) and the PSD (right) of the micro-scale at three time steps

Fading statistics are plotted against the elevation angles in Figure 4.6, where again each curve represents one link. The fractional fade time and the number of fades behave similarly, which is expected, as the fractional fade time is defined as the fraction of fades in one microscopic population, described in algo. 2. Erratic behaviour starts approximately below 100 fades for all links, after which all statistics diverge. Before this threshold, the mean fade time decreases with increasing elevation, from around 200 ms to 1 ms. This is expected as higher elevation induces weaker turbulence with a higher frequency (Figure 4.4). resulting in both weaker and shorter fades.

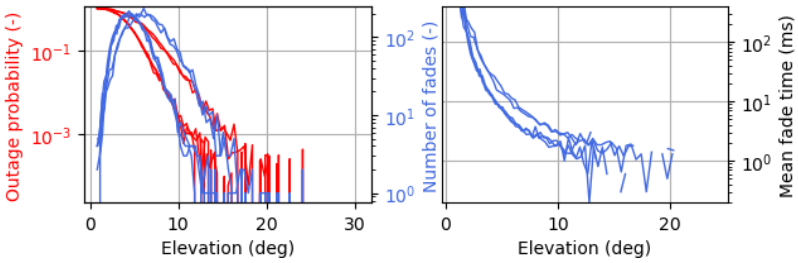

Figure 4.6: Fractional fade time (left), number of fades (left) and mean fade time (right) of each microscopic evaluation

4.3 Comparison with literature

The results of our end-to-end model are compared to existing models in literature and measurements from experiments. This is done for both the macro-scale and micro-scale results.

4.3.1 Macro-scale

The average channel capacity of a communication link between an aircraft flying at 10 km and a LEO constellation is modeled by [21] using a probability model. It estimates a capacity of 16.2 Gbps for a constellation at 1200 km altitude, which is lower than the average capacity of 29.3 Gbps in Figure 4.3. This is is likely due to the lower carrier frequency of [21] or the fact that [21] permits negative elevation angles down to -3°. Looking at RF systems, the throughput per receiver gateway antenna for the initially deployed Starlink constellation is approximately 7.1 Gbps [4] without ISL. Looking at the capacity in Figure 4.3, this can be well exceeded by our model, as expected for FSO systems. The modeled throughput for the uplink in Figure 4.3 is set at 2.5 Gbps, but the P_{RX} margins in Figure 4.3 indicate that higher throughput is possible.

Due to a lack of link budget models regarding the selected ASL use case, the link budget in Table 4.1 is compared to a ground-to-GEO model in [13]. Considering the difference in the use cases, the models agree well with each other, except for three observations. (1) A ground-to-GEO uplink has a much smaller beam divergence in order to decrease the free space loss (289.7 dB), as opposed to our case of aircraft-to-LEO links, where a larger beam divergence is preferred to alleviate pointing errors. (2) Atmospheric attenuation is similar for both cases, except for the cloud losses, which are less significant for ASL. (3) The turbulence effects of beam wander, scintillation and WFE in [13] are more severe (-8.6 dB) due to the highly turbulent boundary layer below 2 km, as opposed to the

weak turbulence in ASL due to high altitudes. However, our model shows a higher total turbulence loss due to the power penalty, which leads to believe that our model is stricter.

4.3.2 Micro-scale

The results of this study show similarity with the Power Vector Geneneration tool (PVGeT) developed by Deutsches Zentrum für Luft- und Raumfahrt (DLR), to analyse LEO-to-ground downlinks [7, 53]. Here, unstable behaviour is also visible for strong fades, due to insufficient statistics. The simplification of a flat spectrum in Figure 3.4 doesn't lead to large difference of temporal behaviour compared to [7, 53]. For a LEO-to-ground downlink correlation times of 1.2 ms are measured (where the auto-covariance function has decreased to 50%) [53]. This is slightly lower than the simulated correlation time of 2.5 ms at 10° Figure 4.5, which is expected due to a higher wavelength in [53]. When increasing the elevation, the correlation time decreases to 1.5 ms due to increasing transverse wind speeds (Equation 3.15), as expected.

Measurements during the LOLA mission, an air-to-GEO uplink [54], show a BER range of 10^{-2} to 10^{-7}, which is roughly equal to the simulated BER at an elevation between 10° to 20° in Figure 4.3. Where the BER time series in [54] is constant due to a constant elevation in GEO, the simulated BER shows much better performance at higher elevation. This comparison is realistic as the LOLA mission is performed at a lower aircraft altitude of 9 km and with a larger propagation path of 40.000 km. Furthermore, P_{RX} measurements of a LEO-to-ground downlink in [55] show very similar behaviour of the power scintillation index with varying elevation, compared to our model, taking into account slightly lower values in [55] do to stronger turbulence.

Chapter 5

Conclusion

An FSO communication mission with a satellite constellation involves multiple physical processes defined at four time scales. Firstly, there are (1) platform dynamics, with a frequency of minutes to hours. Secondly, considering a LEO constellation there is a (2) link frequency of 5 to 10 min, where atmospheric attenuation occurs. At lower time scales, (3) atmospheric turbulence and platform vibrations occur between each 1 to 100 milliseconds, and (4) bit transportation and processing occur in the order of nanoseconds. A model is proposed that integrates all the above processes, such that it can model such a mission end-to-end. This model can prove useful for the analysis and verification of complete GSL, ASL and ISL missions, and helps increase our knowledge of the combined physical processes during these missions. A use case of an ASL mission is chosen in this study in order to investigate the communication potential between aircraft and satellites. A modular design approach aids a model extension to the other mission use cases.

To integrate the above processes and model a satellite communication mission end-to-end, the MMM is proposed, which combines the TPCWM and the HMM. Submodels have been developed and verified for each process and connected in the multi-scale framework. Convergence analysis is performed with respect to the most critical model parameters. Finally, the model is demonstrated with a test case consisting of an aircraft flight route between two airports in Norway and a polar-orbit constellation at 1200 km altitude.

This demonstration shows that a numerical simulation of a 1.5-hour mission takes approximately 6 minutes with 8 GB RAM using a normal PC. Macro-scale platform dynamics and micro-scale platform jitter are the most dominant effects with respect to communication performance for ASL links. Updating the macro-scale solution with the micro-scale solution results in a signal power difference of 10dBW to 80dBW, depending on the strength of the atmospheric channel.

The model is not yet validated with respect to experimental data due to a lack of historical demonstrations. However, the end-to-end model shows realistic output of the mission performance metrics when compared to other models and measurements. It also allows insight into the dependencies between the macro-scale and micro-scale processes.

Bibliography

[1] Hemani Kaushal and Georges Kaddoum. Optical Communication in Space: Challenges and Mitigation Techniques. Tech. rep. 1. Jan. 2017, pp. 57–96. DOI: 10.1109/COMST.2016.2603518.

[2] Morio Toyoshima. "Recent Trends in Space Laser Communications for Small Satellites and Constellations". In: Journal of Lightwave Technology 39.3 (Feb. 2021), pp. 693–699. ISSN: 15582213. DOI: 10.1109/JLT.2020.3009505.

[3] Mark Handley. "Delay is not an option: Low latency routing in space". In: HotNets 2018 - Proceedings of the 2018 ACM Workshop on Hot Topics in Networks. Association for Computing Machinery, Inc, Nov. 2018, pp. 85–91. ISBN: 9781450361200. DOI: 10.1145/3286062.3286075.

[4] Nils Pachler et al. An Updated Comparison of Four Low Earth Orbit Satellite Constellation Systems to Provide Global Broadband. Tech. rep.

[5] Karen Saucke et al. "Characterisation of the optical channel GEO to ground: using five years of data from Alphasat TDP1 and T-AOGS for investigation of different conditions". In: SPIE-Intl Soc Optical Eng, June 2021, p. 211. DOI: 10.1117/12.2600018.

[6] Laserlight data sheet. Tech. rep.

[7] Dirk Giggenbach et al. Reference Power Vectors for the Optical LEO Downlink Channel. Tech. rep.

[8] Ronald Parenti et al. "Modeling the PDF for the irradiance of an uplink beam in the presence of beam wander". In: Atmospheric Propagation III. Vol. 6215. SPIE, May 2006, p. 621508. ISBN: 0819462713. DOI: 10.1117/12.666547.

[9] Morio Toyoshima et al. Optimum divergence angle of a Gaussian beam wave in the presence of random jitter in free-space laser communication systems. Tech. rep. 2002.

[10] Fan Yang, Julian Cheng, and Theodoros A. Tsiftsis. "Free-space optical communication with nonzero boresight pointing errors". In: IEEE Transactions on Communications 62.2 (2014), pp. 713–725. ISSN: 00906778. DOI: 10.1109/TCOMM.2014.010914.130249.

[11] Hristo Ivanov et al. "Testbed Emulator of Satellite-to-Ground FSO Downlink Affected by Atmospheric Seeing Including Scintillations and Clouds". In: Electronics (Switzerland) 11.7 (Apr. 2022). ISSN: 20799292. DOI: 10.3390/electronics11071102.

[12] Mikhail S. Belen'kii, Kevin Hughes, and Vincent Rye. "Free-space laser communication model". In: Active and Passive Optical Components for WDM Communications IV. Vol. 5595. SPIE, Oct. 2004, p. 167. DOI: 10.1117/12.570496.

[13] Ricardo Barrios et al. "Link budget assessment for GEO feeder links based on optical technology". In: International Journal of Satellite Communications and Networking 39.2 (Mar. 2021), pp. 160–177. ISSN: 15420981. DOI: 10.1002/sat.1371.

[14] Dirk Giggenbach, Marcus T. Knopp, and Christian Fuchs. "Link budget calculation in optical LEO satellite downlinks with on/off-keying and large signal divergence: A simplified methodology". In: International Journal of Satellite Communications and Networking (2023). ISSN: 15420981. DOI: 10.1002/sat.1478.

[15] Assyr Abdulle et al. "The heterogeneous multiscale method". In: Acta Numerica 21 (2012), pp. 1–87. ISSN: 14740508. DOI: 10.1017/S0962492912000025. URL: Abdulle.

[16] G. Frantziskonis et al. "Time-parallel multiscale/multiphysics framework". In: Journal of Computational Physics 228.21 (Nov. 2009), pp. 8085–8092. ISSN: 10902716. DOI: 10.1016/j.jcp.2009.07.035.

[17] Airbus en TNO ontwikkelen lasercommunicatieterminal voor vliegtuigen. URL: https://www.tno.nl/nl/newsroom/2021/04/airbus-tno-gezamenlijk-programma.

[18] Jacob Nielsen. "Nielsen's Law of Internet Bandwidth". In: (Apr. 1998).

[19] Otakar Wilfert and Zdenek Kolka. "Statistical model of free-space optical data link". In: Free-Space Laser Communications IV. Vol. 5550. SPIE, Oct. 2004, p. 203. DOI: 10.1117/12.558697.

[20] G. Eswara Rao et al. "Free-space optical communication channel modeling". In: Smart Innovation, Systems and Technologies. Vol. 43. Springer Science and Business Media Deutschland GmbH, 2016, pp. 391–396. ISBN: 9788132225379. DOI: 10.1007/978-81-322-2538-6{_}41.

[21] Niloofar Okati and Taneli Riihonen. "Downlink and Uplink Low Earth Orbit Satellite Backhaul for Airborne Networks". In: 2022 IEEE International Conference on Communications Workshops, ICC Workshops 2022. Institute of Electrical and Electronics Engineers Inc., 2022, pp. 550–555. ISBN: 9781665426718. DOI: 10.1109/ICCWorkshops53468.2022.9814585.

[22] Hachemi Chenina, Djamel Benatia, and MHamed Boulakroune. "New modeling approach of laser communication in constellation and through atmospheric disturbances". In: Bulletin of Electrical Engineering and Informatics 10.4 (Aug. 2021), pp. 2088–2099. ISSN: 23029285. DOI: 10.11591/EEI.V10I4.2792.

[23] Meixuan Li et al. "Random vibration analysis in mechanical environment of satellite laser communication terminal telescope". In: Proceedings - 2020 2nd International Conference on Artificial Intelligence and Advanced Manufacture, AIAM 2020. Institute of Electrical and Electronics Engineers Inc., Oct. 2020, pp. 373–376. ISBN: 9781728199863. DOI: 10.1109/AIAM50918.2020.00082.

[24] Sumit Kumar, Sumit Dalal, and Vivek Dixit. THE OSI MODEL: OVERVIEW ON THE SEVEN LAYERS OF COMPUTER NETWORKS. Tech. rep., pp. 461–466. URL: www.researchpublish.com.

[25] Optical Communications Terminal (OCT) Standard Version 3.0. Tech. rep. 2021.

[26] Dirk Giggenbach et al. Optical on-off keying data links for low Earth orbit downlink applications. Tech. rep.

[27] CCSDS Historical Document. Tech. rep. Washington: CCSDS, 2006. URL: http://public.ccsds.org/publications/.

[28] Arun K. Majumdar and Jennifer C. Ricklin. Free-Space Laser Communications, Principles and Advances. Tech. rep. 2008. URL: http://springeronline.comlseries/4810..

[29] L. Baffico et al. "Parallel-in-time molecular-dynamics simulations". In: Physical Review E - Statistical Physics, Plasmas, Fluids, and Related Interdisciplinary Topics 66.5 (Nov. 2002), p. 4. ISSN: 1063651X. DOI: 10.1103/PhysRevE.66.057701.

[30] Abhijit Chatterjee and Dionisios G. Vlachos. "Multiscale spatial Monte Carlo simulations: Multigriding, computational singular perturbation, and hierarchical stochastic closures". In: Journal of Chemical Physics 124.6 (2006). ISSN: 00219606. DOI: 10.1063/1.2166380.

[31] Weinan E. Principles of Multiscale Modeling. Tech. rep. 2011.

[32] Dominic Dirkx et al. Tudat Space. 2022.

[33] Dominic Dirkx. Tudat mathematical model definition. Tech. rep. 2022. URL: https://tudat.tudelft.nl.

[34] Cho Chang-Hwa. "NORAD TLE TYPE ORBIT DETERMINATION OF LEO SATELLITES USING GPS NAVIGATION SOLUTIONS". In: (2002).

[35] Kelso T.S. CelesTrak. 2023. URL: https://celestrak.org/.

[36] Xavier Olive. "traffic, a toolbox for processing and analysing air traffic data". In: Journal of Open Source Software 4.2475-9066 (2019).

[37] John Stryjewski. Coordinate Transformations. Tech. rep.

[38] Dr.ir. Rudolf Saathof. AE4880 Laser Satellite Communications II. Tech. rep. 2021.

[39] D. Vasylyev, W. Vogel, and F. Moll. "Satellite-mediated quantum atmospheric links". In: (Jan. 2019). DOI: 10.1103/PhysRevA.99.053830. URL: http://arxiv.org/abs/1901.07452%20http://dx.doi.org/10.1103/PhysRevA.99.053830.

[40] L. Phillips Ronald and Larry C. Andrews. Laser Beam Propagation through Random Media. SPIE, 2005. URL: https://ebookcentral-proquest-com.tudelft.idm.oclc.org/lib/delft/detail.action?docID=728499#.

[41] Robert J Noll. Zernike polynomials and atmospheric turbulence*. Tech. rep. 1976.

[42] L C Andrews, R L Phillips, and P T Yu. Optical scintillations and fade statistics for a satellite-communication system. Tech. rep.

[43] Morio Toyoshima et al. "Frequency characteristics of atmospheric turbulence in space-to-ground laser links". In: Atmospheric Propagation VII. Vol. 7685. SPIE, Apr. 2010, 76850G. ISBN: 9780819481498. DOI: 10.1117/12.850149.

[44] N. Perlot et al. "Results of the optical downlink experiment KIODO from OICETS satellite to optical ground station Oberpfaffenhofen (OGS-OP)". In: Free-Space Laser Communication Technologies XIX and Atmospheric Propagation of Electromagnetic Waves. Vol. 6457. SPIE, Feb. 2007, p. 645704. ISBN: 0819465739. DOI: 10.1117/12.708413.

[45] Craig Hoyle. "Airbus readies high-flying Zephyr for 2024 service launch". In: (2023). URL: https://www.flightglobal.com/defence/airbus-readies-high-flying-zephyr-for-2024-service-launch/151546.article.

[46] Morio Toyoshima et al. "Ground-to-satellite laser communication experiments". In: IEEE Aerospace and Electronic Systems Magazine 23.8 (Aug. 2008), pp. 10–18. ISSN: 08858985. DOI: 10.1109/MAES.2008.4607894.

[47] Philippe Gallion. Basics of incoherent and coherent digital optical communications. Tech. rep. 2016.

[48] Hamid Hemmati. Deep Space Optical Communications. Tech. rep. 2004.

[49] Biswanath Mukherjee. Free Space Optical Communication. Tech. rep. 2017. URL: http://www.springer.com/series/6976.

[50] Arun K. Majumdar. Laser Communication with Constellation Satellites, UAVs, HAPs and Balloons. Springer International Publishing, 2022. DOI: 10.1007/978-3-031-03972-0.

[51] Recommendation for Space Data System Standards TM SYNCHRONIZATION AND CHANNEL CODING RECOMMENDED STANDARD BLUE BOOK. Tech. rep. Washington: CCSDS, 2022.

[52] Dirk Giggenbach. "Fading-loss assessment in atmospheric free-space optical communication links with on-off keying". In: Optical Engineering 47.4 (Apr. 2008), p. 046001. ISSN: 0091-3286. DOI: 10.1117/1.2903095.

[53] Dirk Giggenbach et al. "Power vector generation tool for free-space optical links - PVGeT". In: 2017 IEEE International Conference on Space Optical Systems and Applications, ICSOS 2017. Institute of Electrical and Electronics Engineers Inc., May 2018, pp. 160–165. ISBN: 9781509065110. DOI: 10.1109/ICSOS.2017.8357228.

[54] Vincent Chorvalli et al. "Optical communications between an aircraft and a geo relay satellite: design and flight results of the LOLA demonstrator". In: SPIE-Intl Soc Optical Eng, Nov. 2017, p. 10. ISBN: 9781510616219. DOI: 10.1117/12.2308195.

[55] Florian Moll et al. “LEO-ground scintillation measurements with the optical ground station Oberpfaffenhofen and SOTA/OPALS space terminals”. In: Advanced Free-Space Optical Communication Techniques and Applications II. Vol. 9991. SPIE, Oct. 2016, p. 999102. ISBN: 9781510603868. DOI: 10.1117/12.2254809.

Appendix A

Research Objectives

This thesis research is performed as a collaboration between the TU Delft and Airbus Netherlands and is motivated by the FSO communication service program UltraAir. The research is driven by its two contributions. First, the end-to-end model should be applicable to actual communication missions. Second, the MMM should successfully and efficiently integrate all the defined physical processes that are present in such missions. Based on these drivers, the research objectives are defined, which drive the research direction and function as a reflection of the outcome of the research. The objectives are broken down into lower-level questions as follows:

1. Develop a method that combines all relevant processes within a global free-space optical communication mission between one aircraft and a satellite constellation.
   (a) Which existing methods can be used to integrate all relevant processes [1] separately?
   (b) Which methods can be used to integrate these processes?
   (c) Which methods can be applied to speed up the simulation?
2. Using this method, simulate the performance of such a mission.
   (a) Which metrics should be modeled to obtain useful information for mission analysis?
   (b) How should these metrics be visualized?
3. Allow the model to be extended to ground-to-satellite and inter-satellite missions.
   (a) How can one implement versatility in the model?
   (b) How can one create separate modules for all sub-models in the model?

[1] Relative platform dynamics, satellite handover process, atmospheric attenuation and turbulence, platform vibrations, noise, signal detection and processing.

Appendix B

Multi-scale method

B.1 The Time-parallel compound wavelet method

The TPCWM builds on the time-parallel (Parareal) approach [29]. This approach consists of a coarse-scale solution and a corresponding ne-scale stochastic solution, which is coarse-grained to be consistent with the coarse-scale solution at least to the first order. The coarse-scale solution $\mathbf{y}_{c(n)}$ is generated with a coarse propagator $\mathbf{G}_{\Delta T}$. The fine-scale solution is then generated for each time step $\mathbf{T}_n$, in parallel, with a fine propagator $\mathbf{F}_{\delta t}$. This is represented by the right term of the right side of Equation B.1. Then, the fine-scale solution $\mathbf{y}^k_{f(n)}$ is used to iteratively correct the coarse-scale solution $\mathbf{y}^{k+1}_{c(i)}$ at each time step $\mathbf{T}_n$ in serial, represented by the left term of the right side of Equation B.1.

$$\mathbf{y}^{k+1}_{(n+1)} = \mathbf{y}^{k+1}_{c(n+1)} + \Delta^k_{n+1} = \mathbf{G}_{\Delta T}\left(\mathbf{y}^{k+1}_n\right) + \left[\mathbf{F}\left(\mathbf{y}^k_n\right) - \mathbf{G}_{\Delta T}\left(\mathbf{y}^k_n\right)\right] \tag{B.1}$$

The disadvantage of the time-parallel approach is that the fine-scale solution is to be propagated for each time segment $\Delta\mathbf{T} = T_{n+1} - T_n$, increasing the computational cost considering very fine-scale processes. To alleviate this problem, a compound wavelet method (CWM) is used. This feature allows the fine-scale solution to be propagated over a fine-scale time interval $\mathbf{t}_{fine}$, then converted to a compound wavelet, described on page 4 in [16], and then used to update the coarse response (the right term of the right side of Equation B.1).
This method is applicable to problems where stochastic fine-scale processes and deterministic large-scale processes have to be coupled [16]. Our model consists of stochastic turbulence and jitter processes at micro-scale level and all other processes are considered deterministic, making this method suitable for the model. However, there are numerous disadvantages. First, the fine-scale solution is assumed to be stationary at each fine-scale time interval $\mathbf{t}_{fine}$, which doesn't necessarily have to be a disadvantage but might become a problem for highly dynamic problems. Second, first-order similarity is required between the coarse grained $\mathbf{y}_{f(n)}$ and $\mathbf{y}_{c(n)}$. Atmospheric

turbulence may have a significantly large effect on the solution in strong turbulence regimes. Due to its highly stochastic nature, it is difficult to estimate its degradation effects in the coarse-solution and thus this first-order similarity cannot be guaranteed. Finally, a combination of both the time parallel approach of [29] and the CWM of [16] increases complexity. For these reasons, another, less complex model is preferred for our specific problem. However, the notion of the time parallel approach will be used for the simulation of the macro-scale and micro-scale processes in our model.

B.2 The Coarse-grained Monte Carlo method

The CGMCM method uses a statistical framework that combines variables of microscopic processes with variables of macroscopic processes with a coarse-graining method. First, the microscopic processes are simulated with a lattice grid, where each cell in the grid represents the probability of occupancy of that cell. The processes at this level are assumed Markov random fields, meaning that these are ultimately stochastic processes. As visualized in Figure B.1, coarse graining is performed by using stochastic closures of a group of cells.
The two requirements of a suitable application are (1) clear time scale separation and (2) a very large macro-scale domain. The former is defined by local equilibrium of microscopic processes over short time intervals. The latter results from the fact that a stochastic approach requires sufficient statistical data. First, [30] states that the method can be extended to multiple time scales. However, the macroscopic time scales in our model (mission level and link level) are quite close and a clear-cut separation might thus be difficult. Additionally, due to its inherently stochastic approach with Markov random fields, this method is less suitable for the deterministic processes in our model. Therefore, another method is preferred for our problem.

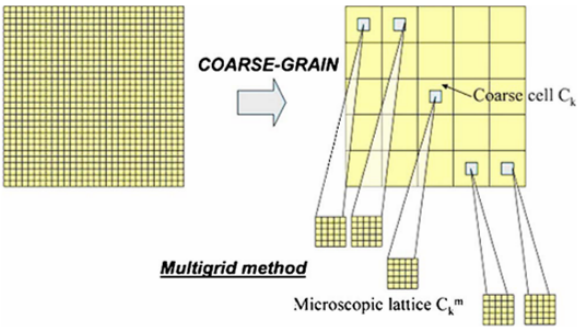

Figure B.1: A visualization of the CGMC method, with courtesy from [30]

B.3 Heterogeneous Multi-scale Method

The Heterogeneous multi-scale method (HMM) is a generic approach to combining multiple time scales, typically used for problems containing ordinary differential equations (ODE) or molecular models [15]. A more detailed explanation of the basic steps of the HMM is as follows:

1. Simulating macro-scale behaviour
   For macroscopic time step $\mathbf{T}_i$, the macroscopic state $\mathbf{U}^T$ is simulated.
   $$T = T_{begin}, T_{begin} + \Delta T, \dots, T_{end} \tag{B.2}$$
2. Simulating the micro-scale behaviour
   Using local constraints of $\mathbf{U}^T$, the microscopic state u_t is simulated at each microscopic time step t for a total of M steps.
   $$u^{n,m+1} = S_{\delta t}(u^{n,m}; U^n), t = 0, \Delta t, \dots, M-1 \tag{B.3}$$
3. Processing data
   The microscopic data is processed with operator $\mathbf{D}_M$ such that it can be used for the macroscopic solver. Here, an averaging method can be used for example.
   $$D^n = D_M(u^{n,0}, u^{n,1}, \dots, u^{n,M}), \tag{B.4}$$
4. Simulating the macro-scale behaviour
   Using the data D^n, the macroscopic state U^n is propagated to time step $n+1$.
   $$U^{n+1} = S_{\Delta t}(U^n; D^n) \tag{B.5}$$

Figure B.2 shows the interaction between the macro-scale domain and the micro-scale domain. Due to its generic approach, this method can be reshaped such that it can fit a specific problem, making the method suitable for our model. Furthermore, its versatility also allows for any modifications of the model in case of extension to other missions, such as GSL or ISL. However, step 4 of the HMM uses a serial propagation operator $S_{\Delta t}$ of the macro-scale solution, where each time step is evaluated with information of the former time step. This reduces the performance in terms of efficiency. By combining the HMM with the TPCWM, a time parallel approach can be used instead of the serial approach, increasing efficiency.

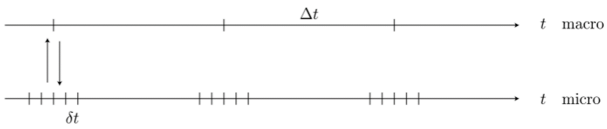

Figure B.2: Visualization of HMM, with courtesy from [15]

B.4 Sequential modeling

An analysis is performed to check the feasibility of this method. This is done for 1 aircraft-to-satellite link. The micro-scale model is decoupled from the macro-scale model and simulated separately. The micro-scale model depends on $\mathbf{m}$ macroscopic variables, thus the micro-scale simulations have to be performed with constraints of these $\mathbf{m}$ variables. To accurately map the micro-scale model to the macro-scale model, the micro-scale simulation is performed over a range of values of each of the $\mathbf{m}$

variables.

Table B.1 shows the microscopic variables that are a function of the macroscopic variables. The state of the satellites (position and velocity) has a significant effect on the wind speed, through the slew rate, and thus on the cut-off frequency of turbulence ω_t. The aircraft state has the same effect through its cruise speed, but also its altitude significantly affects the turbulence strength through C_n^2 and r_0. Then, the slant range naturally influences P_{RX} through the free space loss h_{fs} and the attenuation loss h_{att}. Additionally, this range also affects the turbulence strength and frequency, as the speckle size at the receiver increases with an increasing slant range. Furthermore, cloud losses are currently a static loss, but adding a time-dependent cloud distribution to the macro-scale model will affect P_{RX} at micro-scale due to varying losses. Finally, the data rate is currently fixed too, but changing this to a varying data rate will affect the bandwidth filters B_o, B_e at the receiver as well as the noise σ_n. For a preliminary analysis, only the slant range is taken as a constraint over which we simulate the micro-scale model.

Macro variable	Dependent micro variable
Satellite states	v_{rms}, ω_t
Aircraft state	v_{rms}, C_n^2, ω_t
Slant range	P_{RX}, C_n^2, r_0, ω_t
Clouds	P_{RX}
Data rate	B_o, B_e, σ_n

Table B.1: Dependent variables

The macro-scale model is simulated once, obtaining the macro-scale solution. The micro-scale model is simulated for multiple steps of the slant range, after which the micro-scale solution (the fine solution) is mapped on the macro-scale solution (the coarse solution). To analyse the sensitivity of step sizes, multiple simulations are performed, each with a different step size. Figure B.3 shows this sensitivity. It can be seen that the mapping becomes less accurate in the low-elevation regime. When using small step sizes, however, a mapping accuracy of less than 0.25 dB of P_{RX} can be achieved. However, around 1.500 micro-scale evaluations are needed here. Assuming 10 links and 5 macroscopic variables instead of one, this amounts to 75.000 micro-scale evaluations for a complete mission.

[1]step 4 covers the results of a full simulation, covered in chapter 4

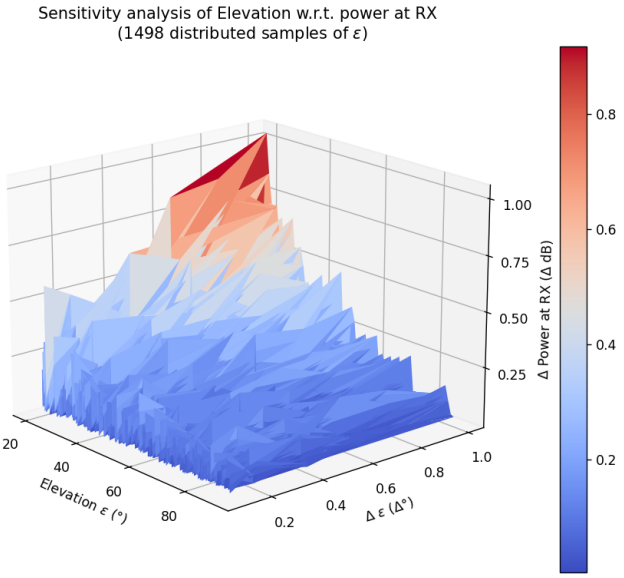

Figure B.3: Sensitivity analysis of the mapping of the micro-scale solution onto the macro-scale solution of the sequential method

To reduce this, micro-scale simulation can be performed with larger step sizes and then interpolated, which is done for BER in Figure B.4, where cubic spline interpolation is used. This works well for the uncoded BER. When introducing non-linearities to the solution, which is the case with the coded BER, cubic spline interpolation is not sufficient anymore. Hence, the required interpolation method in case of additional non-linearities likely becomes costly. To conclude, this method is deemed insufficient for this specific problem, because many evaluations are required due to many dependencies between the macro-scale and the micro-scale model. Interpolation could mitigate this problem but could become costly itself when non-linearities are added to the model, such as FEC coding.

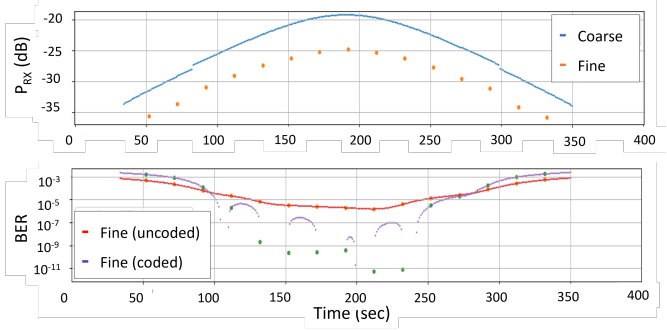

Figure B.4: Macro-scale solution of P_{RX} and BER, using the sequential method with interpolation

Appendix C

Verification

C.1 Strategy

The verification strategy for the model is set up as shown in Figure C.1. Integration happens in steps 1 and 2. All sub-models are first verified separately in step 1. Then, the sub-models are integrated at macro-scale level as well as micro-scale level. These steps discussed in section C.2, C.3 and C.4. After integration, steps 3 and 4[1] are performed for the full model, where a specific mission use case is selected. Step 3 covers a convergence analysis of the model, discussed in section C.5. All identified verification tests for steps 1 and 2 are shown in Table C.1.

C.2 Mission and Link level

C.2.1 SC propagation

The chosen satellite constellation, used in the case study in chapter 4, is tranche 0 of the the constellation operated by SDA. As it is planned to operate as the first optical constellation with uplinks and downlinks, it is considered a representative case. This constellation consists of 2 planes with 14 satellites in each plane. The 2 planes are equidistantly divided by separating the right ascension of the ascending node (RAAN) by 180°. Each satellite in a plane is equidistantly divided with a true anomaly difference of 25°. The propagated Kepler elements of this orbit are plotted in Figure C.2. The fluctuations are caused by the Earth's J2 term.

Looking at the research objectives, the drivers of the verification of the propagation model are speed and accuracy. However, the sensitivity of the satellite state is considered quite low with respect to the link performance, as a positional error will result in a very small error of the free space loss. With this in mind, the simplest model is chosen, while still maintaining sufficient accuracy. Three aspects are analyzed: The type of integrator, the acceleration model and the propagation step size. Fixed step Runge-Kutta 4 (RK-4) and Runge-Kutta 7 (RK-7) are considered. First the minimum allowable step sizes are determined for both integrators by comparing a simulated unperturbed orbit with a theoretical Kepler orbit, which is done for a satellite from the constellations of Starlink and SDA. The magnitude of the largest positional error between the Kepler orbit and the simulated unperturbed orbit is plotted in Figure C.3a and Figure C.3b. It shows that the accuracy increases (error decreases) with a decreasing step size up to the point that erratic behaviour starts. This region should be avoided as it is unpredictable due to dominant rounding errors. At larger step sizes, the truncation error is dominant. For the SDA satellite, the minimum step size is around 7 seconds and 50 seconds for RK-4 and RK-7, respectively. For the Starlink satellite, this decreases slightly to 5 seconds and 43 seconds. This is due to larger dynamics at a lower altitude of 550 km instead of 1000 km for SDA, which enhances the effect of the truncation errors.

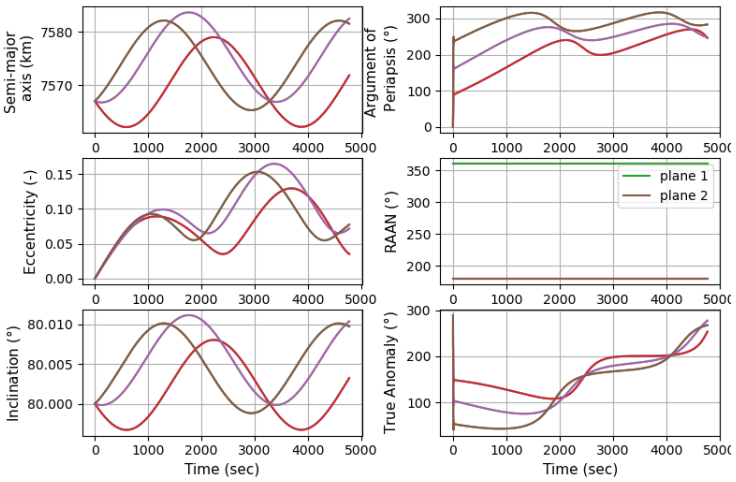

Figure C.2: Kepler elements of 3 satellites from the SDA satellite constellation

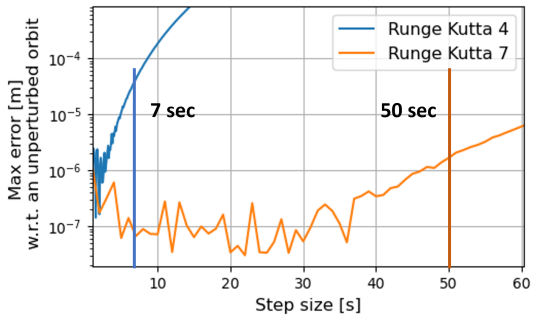

(a) Satellite of SDA tranche 0 constellation

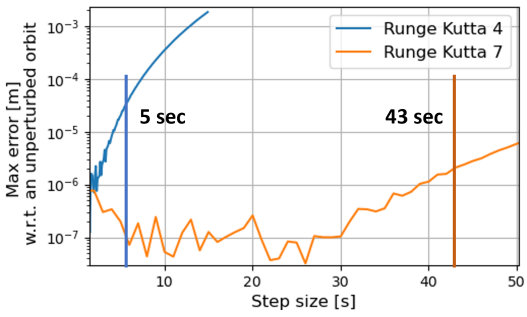

(b) Satellite of Starlink constellation

Figure C.3: A minimum step size analysis for an unperturbed Earth orbit for 2 cases RK-4 and RK-7 for the orbits of SDA and Starlink.

For the selection of an acceleration model, the sensitiv-

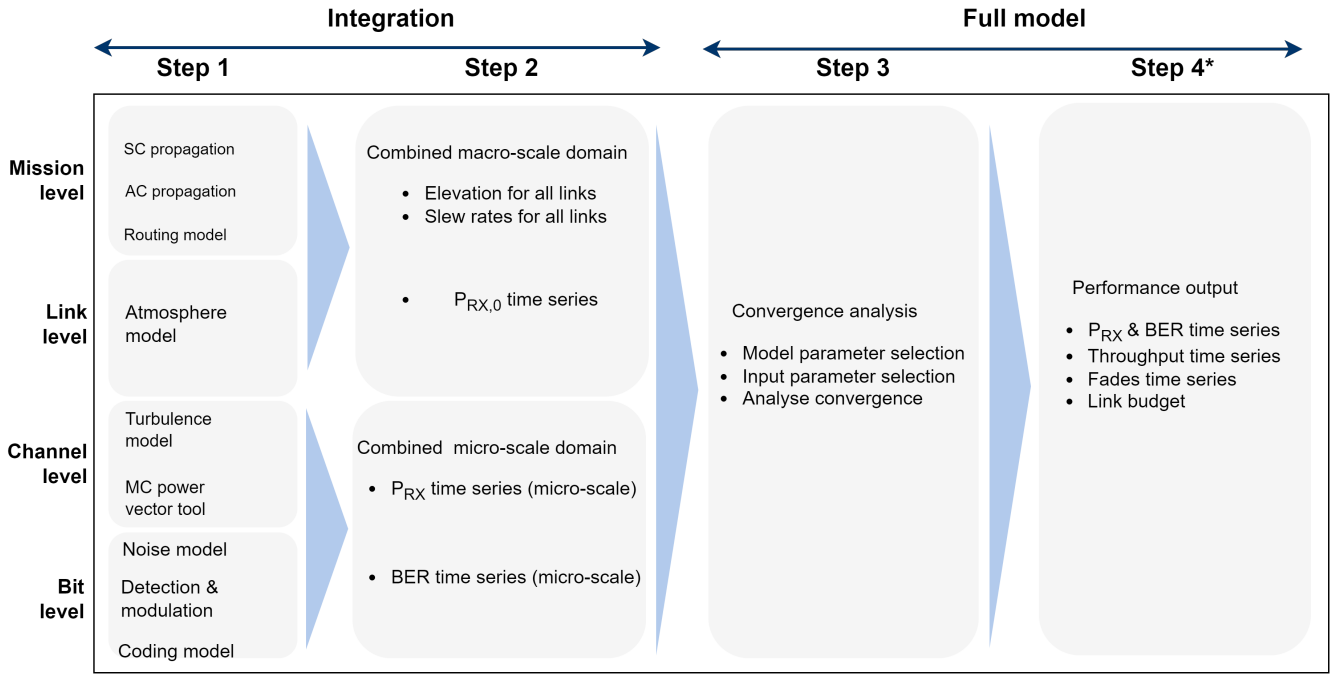

Figure C.1: Overview of the integration steps taken during verification of the sub-models. First, each sub-model is verified separately, as is shown in Table C.1. Then, they are integrated and verified again.

ity of the most dominant acceleration terms is analyzed. For this, we start with a single Earth point-gravity acceleration $\mathbf{a}_{pm}$. Each acceleration is then analyzed by extending $\mathbf{a}_{pm}$ with this acceleration and comparing the new acceleration with the old $\mathbf{a}_{pm}$ in terms of the positional difference (magnitude). The SDA constellation is chosen, as this is also used for the results in chapter 4. This can be seen in Figure C.5a and Figure C.5b.

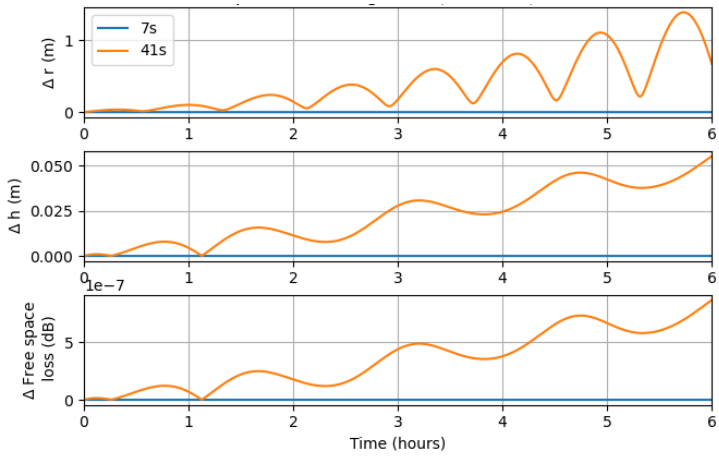

Figure C.4: Comparison of the integrators RK-4 and RK-7 with their corresponding minimum step sizes

Figure C.5b shows the sensitivity of the third body terms of the moon, Mars, Moon, Sun and solar radiation. Figure C.5a shows the sensitivity of Earth's most dominant gravitational anomalies through the terms of the spherical harmonics. These are compared to the J2 term in order to better visualize their effects. The J2 term itself has the largest effect, equaling a maximum of 150 km, and is added to the acceleration model. All other terms are neglected due to their small influence. All spherical harmonic terms except for J2 don't exceed 1 km positional difference, equaling 0.005 dB free space loss. The third body terms and solar radiation don't exceed a positional difference of 12.5 m, equaling 0.0006dB free space loss.

Finally, the integrators are compared with each other by propagating a SDA satellite and plotting the magnitude of the positional difference between the two propagations. This is done with the minimum step sizes for each integrator. From Figure C.4 a maximum positional very difference of 1 m is observed. Due to negligible difference between the two integrators for this type of orbit, RK-4 is selected, as it is less computationally costly.

C.2.2 AC propagation

Aircraft trajectories are extracted from an ADS-B database 'Opensky' [36] as shown in Figure C.6. The counts in the color map indicate the number of ADS-B signals that are transmitted from the aircraft. The dark blue regions of the trajectories have little data with even a few outages (no data transmitted at all), which are visualized as gaps in the trajectory. The flight parameter curves in Figure C.7 can be linearly interpolated to fill these outages and obtain a continuous trajectory.

Table C.1: Verification overview of all sub-models (step 1 and 2 in Figure C.1)

Level	Sub-model	Verification
Mission	SC propagation	• Sensitivity of accelerations • Accuracy of integrator and step size • Visualization of constellation: Kepler elements plot • Visualization of constellation: 3D trajectory
	AC propagation	• Visualization of flight route: 2D on earth map • Accuracy of interpolation • Transformation from ECEF to ECI
	Routing model	• Plot 3D trajectories • Verify link times and number of links • Verify acquisition time
Link	Atmospheric model	• Comparison of ISA model with literature [39]
Combined		• Verify elevation and slew rate for all links • Visualize $P_{RX,0}$ time series • Comparison of static link budget with literature [52]
Channel	Turbulence model	• Check Bufton wind speed model behaviour for different altitudes and air speeds • Comparison of Hufnagel-Valley model for C_n^2 with literature [42] • Comparison of turbulence frequency with literature [43] • Comparison of all variances (intensity, power and displacement) with literature [42] [8] • Analyse all turbulence parameters for different elevation angles, uplink and downlink
	MC Power vector tool	• Verify numerical distributions with theoretical values • Verify PSD and Fourier-transform of all numerical distributions • Verify validity of sum of distributions TX and RX • Verify validity of product of distributions h_{tot} • Analyse all turbulence fluctuations for different elevation angles
Bit	Noise model	• Visualization of noise contributions: Plot over range of P_{RX} dummy data
	Detection & Modulation	• Visualization of BER: Plot against SNR and P_{RX} for each detection and modulation combination • Comparison of BER and SNR with literature [28, 47] • Comparison of preamplifier effect (gain and noise factor) with literature [47]
	Coding model	• Comparison of Reed-Solomon model with literature [26, 51]
Processing	Fading statistics Power penalty	• Verify statistics over a small time series • Comparison of penalty and scintillation index with literature [52]
Combined		• Visualize P_{RX} time series • Visualize BER time series

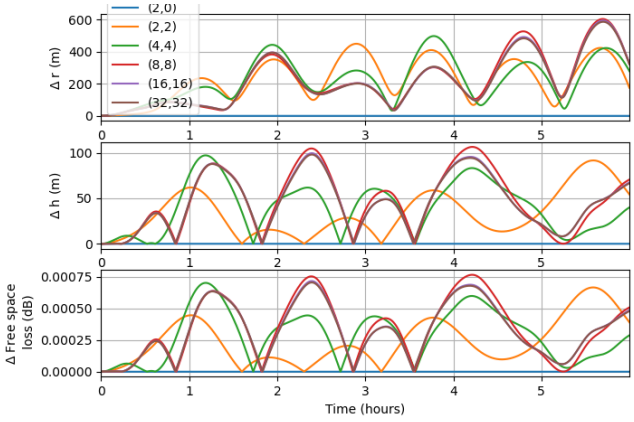

(a) Acceleration terms of Earth spherical harmonics

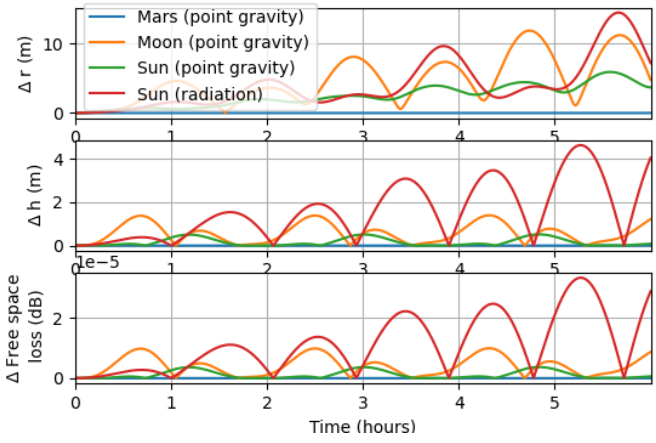

(b) Acceleration terms of Moon/Mars/Sun 3^{rd} body and Sun radiation

Figure C.5: Sensitivity analysis of acceleration terms

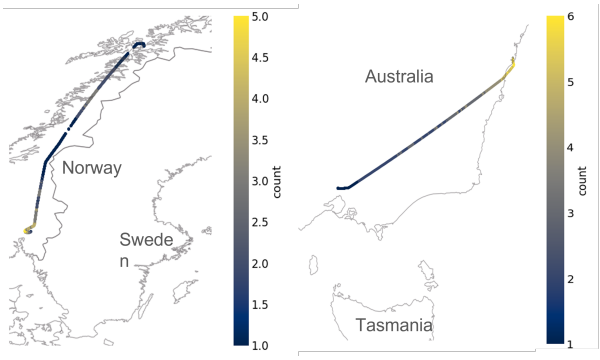

Figure C.6: Aircraft trajectories of Oslo-Eneves (left) and Sydney-Melbourne (right)

In order to obtain the relative geometry between the propagated aircraft and the satellites, all vehicles need to be in the same coordinate system. For this reason, the aircraft state is transformed from the Earth-Centered-Inertial (ECI) coordinate system. As the state is origi-

nally expressed in the longitude, latitude, altitude (LLA) coordinate system, first a transformation is performed from LLA to Earth-Centered-Earth-Fixed (ECEF), and then from ECEF to ECI. Figure C.8 shows the aircraft trajectory in the ECEF system and the ECI system. As expected, the ECEF trajectory is shifted towards the right relative to the ECI trajectory, as the ECEF system includes the rotational spin of the earth. The magnitude of the positional difference is 802.7 km.

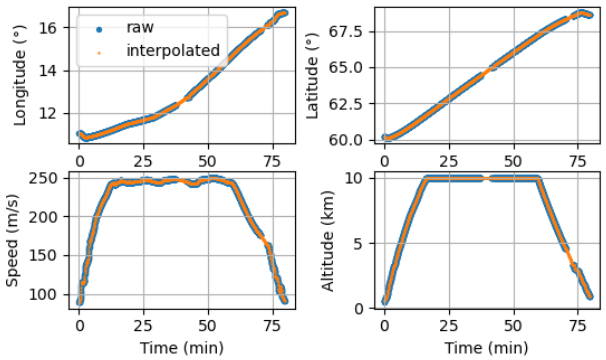

Figure C.7: ADS-B parameters from flight route Oslo-Eneves (Raw data and linearly interpolated data)

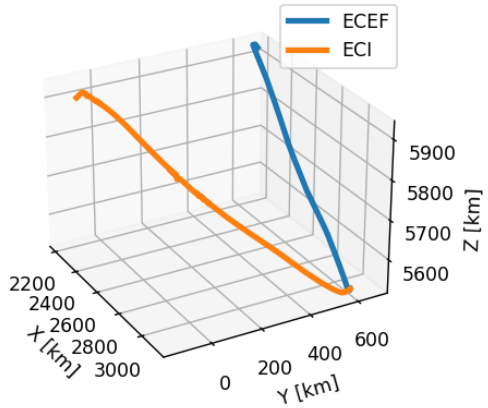

Figure C.8: The same trajectory of the Oslo-Eneves flight route in the ECEF and ECI coordinate system.

C.2.3 Routing model

The routing model uses the algorithm as seen in algorithm 1. To maximize the insight of these verification steps, two existing constellations are modeled: Starlink and OneWeb. The trajectories of the satellites are extracted from TLE data from Celestrak [celestrak] and propagated in Tudat. Figure C.9 shows the link selection between one aircraft, flying from New York to Los Angeles, and OneWeb (Figure C.9b) or Starlink (Figure C.9a). The routing model optimizes the link time in combination with the highest elevation overpass. Looking at OneWeb, all links are approximately the same length, due to the minimum elevation constraint of 0° and the fact that each linked satellite moves approximately in the same direction north, due to the polar orbits. Starlink contains more links that are shorter.

C.2.4 Atmospheric model

The attenuation model is derived from the ISA model [39]. The attenuation in Figure C.10 is plotted against the altitude and follows the same curve as the pressure and number density profiles on page 20 in [39]. This is expected as the method directly relates attenuation to the pressure and number density. The model also depends on the zenith angle, which changes the attenuation as the propagation distance through layers with distinct attenuation coefficient changes. This is also visible in Figure C.10, where larger zenith angles result in larger attenuation.

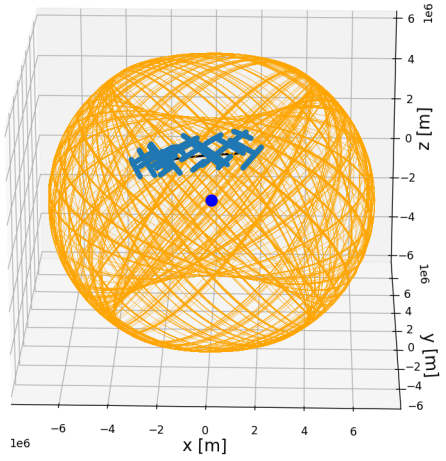

(a) Link selection with Starlink

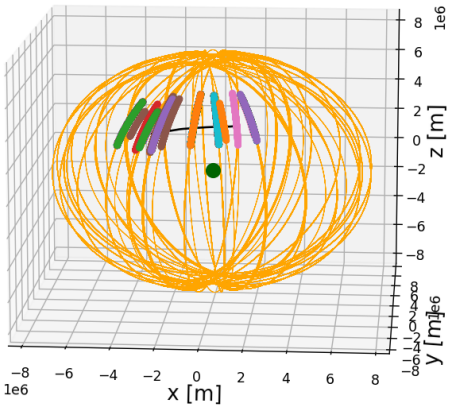

(b) Link selection with OneWeb (500 satellites)

Figure C.9: Constellation trajectories (orange), aircraft route New York-Los Angeles (black) and link selection (colored)

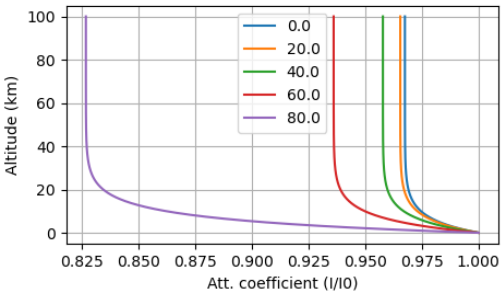

Figure C.10: Attenuation profile based on the ISA model [39]

C.2.5 Combined macro-scale domain

The elevation, slew rate and the signal power $P_{RX,0}$ are analyzed in chapter 4. Figure 4.1b shows distributions of the elevation and slew rate for all links. Figure 4.3 shows a $P_{RX,0}$ time series. A cross-section of $P_{RX,0}$ is elaborated in the link budget in Table 4.1.

C.3 Channel and Bit level

C.3.1 Turbulence model

Wind speed from the Bufton model is plotted against a height profile up to 20 km in Figure C.11 (left) for various aircraft wind speeds and satellite slew rates. The wind speed profile that is used for the turbulence strength (blue line) neglects aircraft speed and slew rate. The wind speed profile that is used for the turbulence cut-off frequency (green and orange lines) includes these terms. Both aircraft speed V_{AC} and satellite slew rate have a significant impact on the RMS of the wind profile V_{rms}. V_{AC} creates an offset of the wind profile and the slew rate tilts the profile upwards, thus having the largest impact at higher altitudes. The corresponding V_{rms} for each wind profile results in different C_n^2 profiles in Figure C.11 (right) with the same colours. When setting the same parameters, it matches the theoretical values as simulated by [40]. V_{rms} has a large effect on the 'bubble' around 10 km altitude both variables have a large impact on the size of the 'bubble' around 10 km altitude. The blue line includes the effect of the Earth's boundary layer, parameterized as term A in the HV model. As it seizes to have any impact above 1 km altitude, this term is neglected in our model.

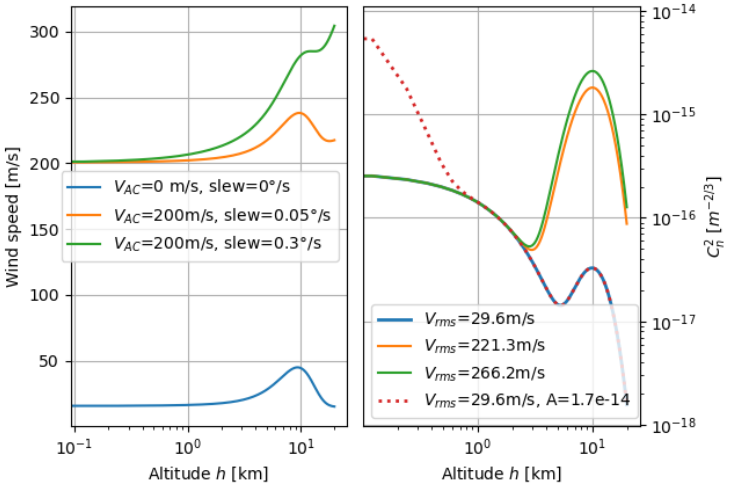

Figure C.11: Wind speed (Bufton model) and C_n^2 (Hufnagel-Valley model)

Regarding scintillation, propagating plane waves are assumed for the downlink and Gaussian waves for the uplink. As mentioned in subsection 3.3.2, the Gaussian assumption is simplified to the limiting case of a spherical wave. Intensity scintillation is computed for weak turbulence theory (Rytov) and a general theory, as proposed in [40]. Then, the power scintillation index σ_P^2 is computed using an aperture averaging effect, described in [40]. Figure C.12a shows the behaviour of these types of scintillation for both uplink (top) and downlink (bottom). When setting the same parameters, it matches the theoretical values as simulated [40]. The weak theory gives the same scintillation index as the general theory up to 83°, indicating a weak turbulence regime. Furthermore, the power scintillation index is almost identical for the uplink, indicating the negligible aperture averaging effect. This is not the case for the downlink. A more detailed analysis in Figure C.12b shows indeed that aperture averaging for the uplink becomes non-negligible for receiver apertures above 30 cm. For the downlink, our selected receiver aperture of 8 cm already shows significant aperture averaging effects.

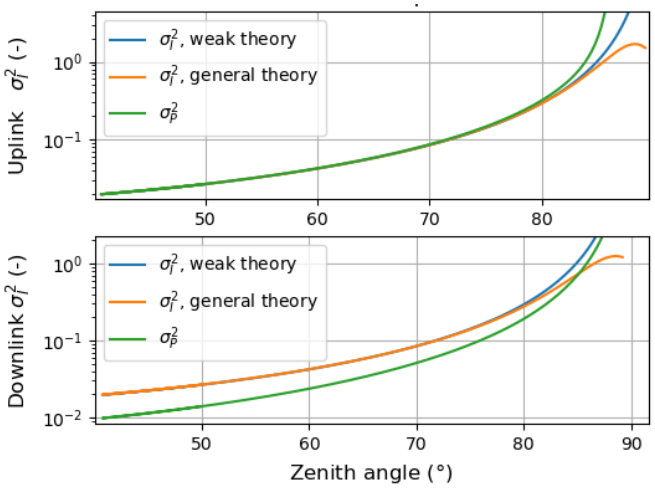

(a) Scintillation index (intensity and power) for weak and strong turbulence theory, for uplink and downlink

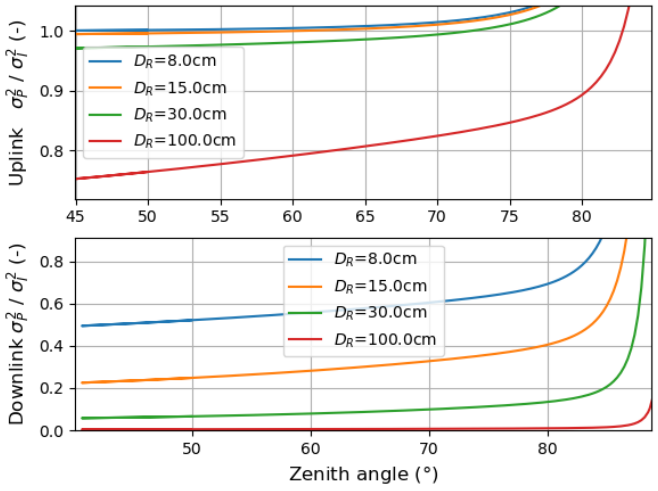

(b) Power vs. Intensity scintillation

Figure C.12: Scintillation index for various zenith angles

As shown in Figure C.13, the spectrum of the signal intensity due to turbulence varies for different elevation angles. An increase in cut-off frequency for higher elevation angles results in a spectrum shift to the right. This change is caused by the transverse wind speed and the speckle size, as defined in Equation 3.15. An increase in elevation results, and thus a longer slant range, results in a larger speckle size and thus lower frequency. However, the influence of the wind speed is much higher at a cruise speed

of around 250 m/s (Figure C.7, leading to an increase of the cut-off frequency. This is confirmed by Figure C.14, where an increase in both transverse wind speed and cut-off frequency is observed. At 0° elevation, aircraft speed has no contribution and in the transverse wind speed in Equation 3.13.

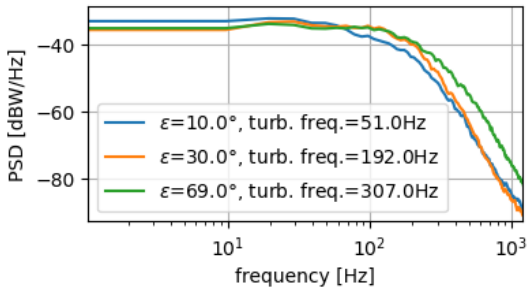

Figure C.13: PSD of power scintillation

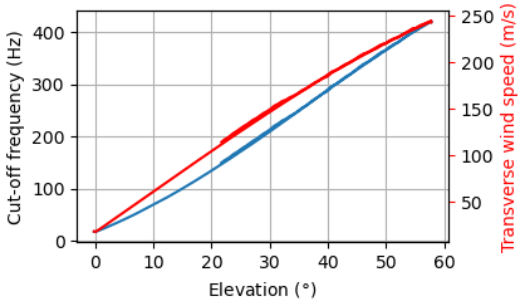

Figure C.14: Turbulence cut-off frequency and transverse wind speed versus elevation

Turbulence model parameters are computed for various elevation angles and for uplink and downlink in Table C.2. It can be seen that turbulence levels generally decrease with an increasing elevation angle, as expected. Furthermore, downlinks are less distorted than uplinks, mostly due to the lower scintillation. This is also expected, as uplinks already experience distortion in the near field, which can propagate and increase further in the far field. We can see that below 5° elevation, weak turbulence transitions to moderate-strong turbulence (σ_I^2 1) and the assumption of weak turbulence becomes invalid. In this regime, the approximation of the power scintillation index σ_P^2 also becomes invalid. Above 10° elevation, turbulence is weak (σ_I^2 « 1). Here, the relation between σ_I^2 and σ_P^2 agree with Figure C.12a and Figure C.12b.

Table C.2: Turbulence output parameters at three cross sections of the simulation of the case study in chapter 4 with V_{RMS}=29.6 m/s.

Parameter	Uplink			Downlink		
Elevation [°]	5	10	40	5	10	40
Range [km]	3536	3108	1677	3537	1492	1281
r_0 [cm]	24.8	37.1	69.7	24.8	37.1	69.7
σ_I^2 [μrad]	0.86	0.29	0.04	0.71	0.28	0.04
σ_P^2 [μrad]	1.92	0.32	0.04	0.67	0.19	0.02
σ_{BW}^2 [μrad]	10.51	4.44	1.30	0.0	0.0	0.0
σ_{AoA}^2 [μrad]	0.01	0.01	0.01	1.53	1.11	0.65

C.3.2 Monte Carlo Power Vector Tool

The Monte Carlo power vector tool, discussed in subsection 3.3.3, simulates 5 micro-scale effects: Scintillation h_{scint}, beam wander θ_{BW}, angle-of-arrival θ_{AoA}, platform jitter at the transmitter terminal $\theta_{pj,TX}$ and platform jitter at the receiver terminal $\theta_{pj,RX}$. These are generated as distributions and then combined into one loss distribution h_{total}. This process is verified by the following steps:

1. Compare each simulated distribution with its theoretical equivalent, given their statistical moments.
2. Analyze the validity of the sum of distributions. Looking at Equation 3.14, there are four distributions added together: $\theta_{TX} = \theta_{BW} + \theta_{pj,TX}$ and $\theta_{RX} = \theta_{AoA} + \theta_{pj,RX}$. These are verified in terms of their statistical moments and the frequency spectrum.
3. Analyze the validity of the product of distribution. Again looking at Equation 3.14, h_{TX}, h_{RX}, h_{scint} are multiplied to form h_{total}. This product is verified in terms of its statistical moments and the frequency spectrum.
4. The combined distribution of h_{total} is visualized.

To perform step 1, a PDF curve is fitted to the histograms of the simulated distributions and compared to the theoretical PDF. A population size of 5.000 samples (5 seconds) is used. For all turbulence effects in Figure C.15, Figure C.16 and Figure C.17 this is done for various elevation angles. For an increase in elevation, turbulence becomes weaker, causing scintillation PDF to shift to the right and the beam wander and AoA PDF to shift to the right. Furthermore, for all effects, the simulated PDF matches the theoretical PDF. The statistical moments (mean and variance) also match the theoretical mean and variance, except for the scintillation. At high elevation, it matches, but around 10° it starts to differ significantly. As the PDFs match each other well, the difference is likely due to a numerical error in the computation of these moments.

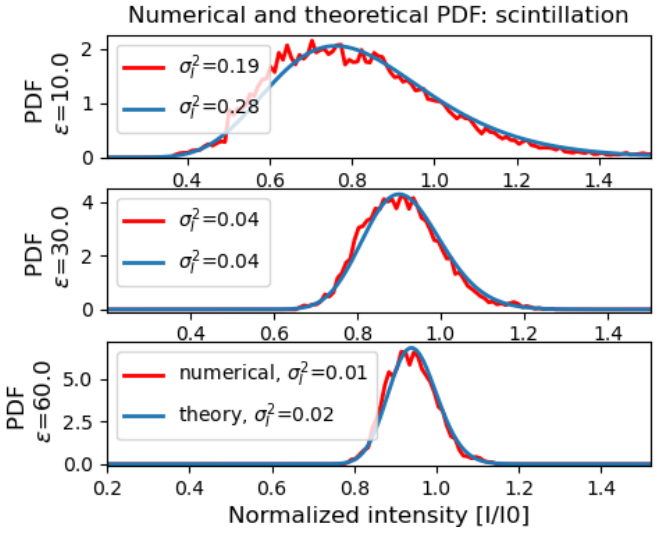

Figure C.15: PDFs of scintillation, log-normal distribution

Sum of distributions

The jitter contributions in TX (beam wander and TX platform jitter), are summed. This is also the case for the RX contributions (AoA fluctuations and RX platform jitter). This is done by summing all discrete random variables of both distributions, as shown in Equation C.1. It is proven that by summing two independent distributions, the mean and variance are also summed, as shown in Equation C.2 and Equation C.3.

$$Z = X + Y \tag{C.1}$$

$$\mu_Z = \mu_X + \mu_Y \tag{C.2}$$

$$\sigma_Z^2 = \sigma_X^2 + \sigma_X^2 \tag{C.3}$$

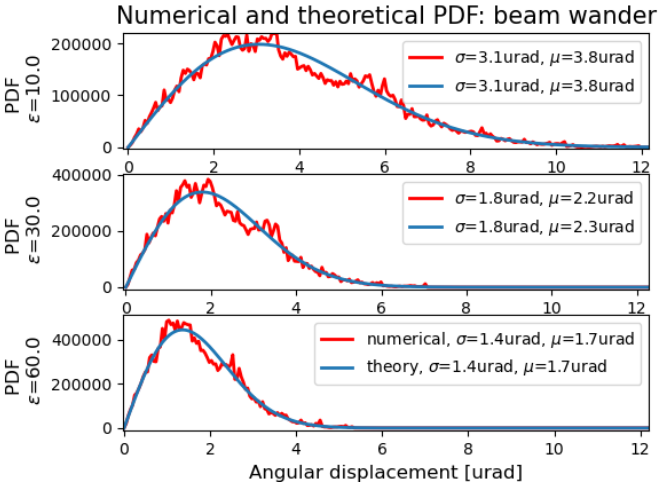

Figure C.16: PDFs of beam wander, Rayleigh distribution

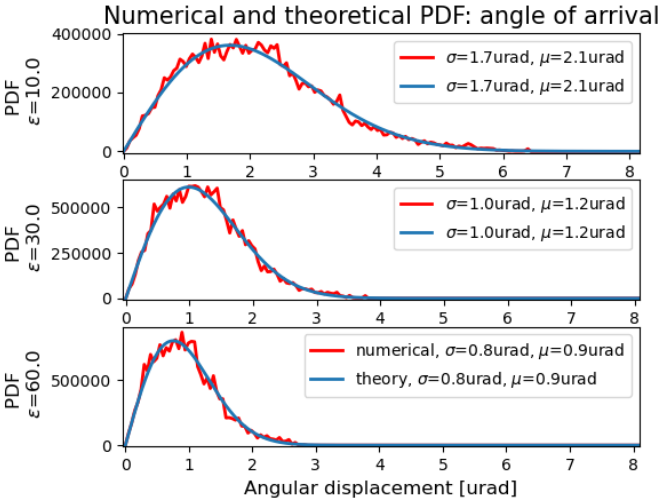

Figure C.17: PDFs of angle-of-arrival fluctuations, Rayleigh distribution

The sum of the distributions is plotted in Figure C.19 and Figure C.20. For the combined TX jitter distribution, the population mean adheres to the requirement posed in Equation C.2, as $\mu_{BW} + \mu_{jitter} = 7.56 + 0.630 = 13.86 = \mu_{TX}$. The population variance also adheres to the requirement in Equation C.3, as $\sigma_{BW}^2 + \sigma_{jitter}^2 = 0.016 + 0.011 = 0.027 = \sigma_{TX}^2$.

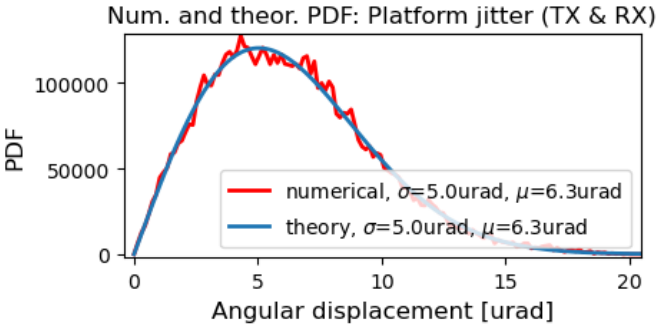

Figure C.18: PDFs of both TX and RX platform jitter, Rayleigh distribution

For the combined RX jitter distribution, the population mean adheres to the requirement posed in Equation C.2, as $\mu_{AoA} + \mu_{jitter} = 0.11 + 6.33 = 6.44 = \mu_{RX}$. The population variance also adheres to the requirement in Equation C.3, as $\sigma_{AoA}^2 + \sigma_{jitter}^2 = 0.0 + 0.011 = 0.011 = \sigma_{RX}^2$.

Product of distributions

After summation of the jitter distributions, they are converted to loss distributions h_{TX} and h_{RX}. Then h_{TX}, h_{RX} and h_{scint} are multiplied, resulting in a product distribution h_{total}. It is proven that the mean of the product of three independent distributions is also the product of the means of the original distributions, as shown in Equation C.4 and Equation C.5, where A is the product. The variance is then equal to Equation C.6.

$$A = X \times Y \times Z \tag{C.4}$$

$$\mu_A = \mu_X \mu_Y \mu_Z \tag{C.5}$$

$$\sigma_A^2 = (\sigma_X^2 + \mu_X^2)(\sigma_Y^2 + \mu_Y^2)(\sigma_Z^2 + \mu_Z^2) - \mu_X^2 \mu_Y^2 \mu_Z^2 \tag{C.6}$$

The histogram of the product distribution h_{tot} is plotted in Figure C.21. The product of the population mean of all three distributions is $\mu_{TX}\mu_{RX}\mu_{scint} = 0.715 \times 0.742 \times 0.888 = 0.497$. This is close to the simulated mean $\mu_A = 0.471$. The difference is caused by the fact the distributions are not completely independent. There are some correlations, because the turbulence effects are present in each distribution, affected by the parameters C_n^2 and r_0. In the case of the variance, the theoretical variance is equal to 0.050 and the simulated variance $\sigma_A^2 = 0.033$. The difference is again likely caused by the fact that there is some dependence between the three distributions, caused by the turbulence correlation.

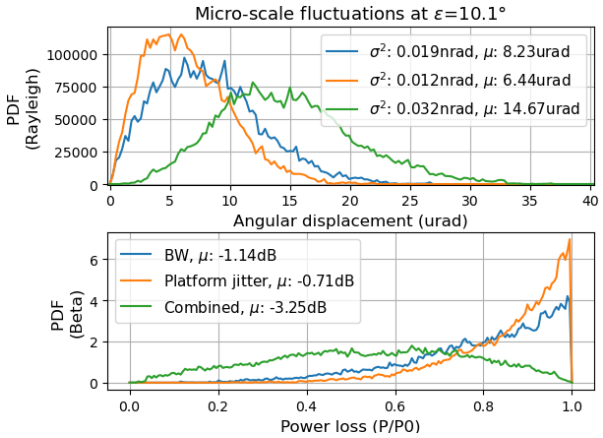

Figure C.19: Sum of the distributions of beam wander and TX platform jitter, resulting in one combined TX jitter distribution

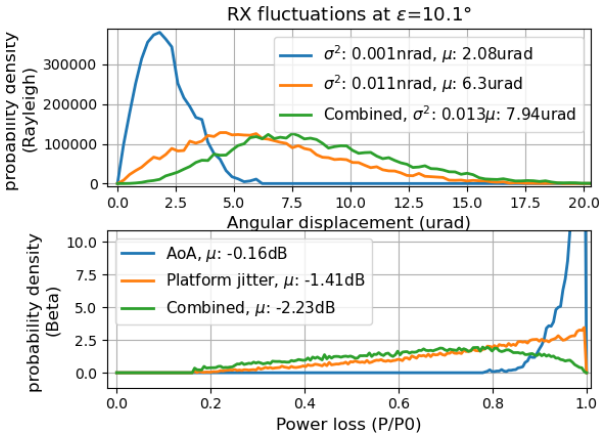

Figure C.20: Sum of the distributions of angle-of-arrival fluctuations and RX platform jitter, resulting in one combined RX jitter distribution

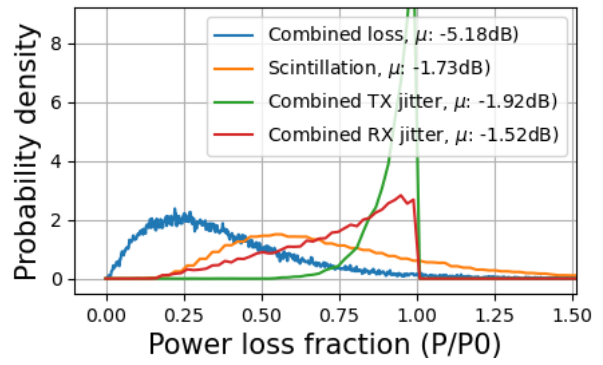

Figure C.21: Product of distributions of h_{TX}, h_{RX} and h_{scint} as defined in Equation 3.14 for an uplink at 20°

C.3.3 Noise model

Shot noise is signal-dependant and increases with increasing P_{RX}. Thermal noise, background noise and beat noise are independent of the signal. Figure C.22 shows these noise types for two APD photo-detectors. They differ through their amplifier, where NF is the noise factor and M is the amplification gain of the amplifier. Shot noise, background noise and beat noise are channel gains and thus dependent increase for a bigger amplifier (right). Thermal noise remains the same, as this noise type is characterized by the terminal itself. This results in a dominant shot noise at higher values of P_{RX}.

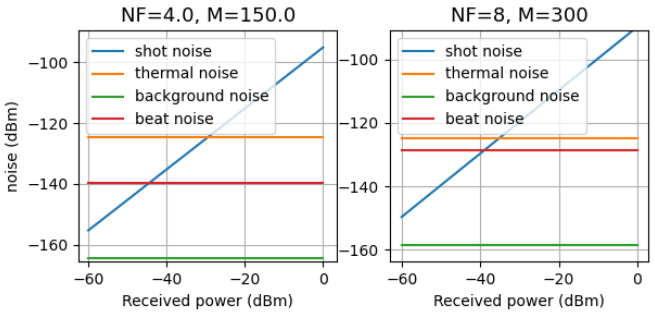

Figure C.22: Noise responses of 2 APD photo-detectors, as a function of P_{RX}

C.3.4 Detection and modulation

The responses of the detection and modulation in Figure C.23 are simulated with the LCT system characteristics shown in Table 3.2. Each cluster represents a detection scheme. The different curves within each cluster represent a different modulation scheme. The PIN detector is thermal noise limited and the quantum-limited detector is shot noise limited. As seen in Figure C.22, the APD detector becomes shot noise limited for high P_{RX}. This is confirmed by the SNR response of the detector in Figure C.23. When $P_{RX} < -30$, the APD follows the same curve as the thermal-limited PIN detector. When $P_{RX} > -30$, the APD follows a quantum-limited detector. The modulation response in Figure C.23 (right) shows that a quantum-limited detector is the most sensitive (low BER output for low P_{RX} input) and the PIN detector is least sensitive, as expected. For each cluster in the modulation response, BPSK is the most sensitive, followed by On-Off keying non-return to zero (OOK-NRZ) and 2-ary pulse position modeling (2-PPM), which are very similar in terms of performance.

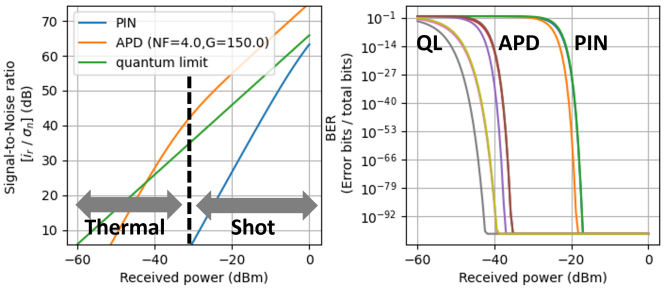

Figure C.23: Visualization of the detection and modulation response: SNR (left) and BER (right) versus P_{RX}. For a PIN and APD detector, and in the quantum limit

C.3.5 Coding model

Approximation of the error mitigation performance of a Reed-Solomon FEC coding scheme, proposed by [27], is plotted in Figure 3.6, subsection 3.4.3. Reed-Solomon FEC coding makes use of an encoder, that converts the bits to code words, and a decoder, that converts the code words back to bits again. A code word contains 255 bits,

of which N information bits, that contain the message. There are $E = 255 - N$ 'extra' parity bits, that can correct erroneous information bits. When decoding the code words of the received signal, three events may happen.

1. All N bits in the code word are decoded correctly. This happens when the number of erroneous bits is less than $E/2$.
2. Erroneous bits are detected, but not corrected. This happens when the number of erroneous bits is more than $E/2$ and less than E.
3. Erroneous bits are not detected and the decoder incorrectly outputs erroneous code words.

Event 2 and 3 may cause the RS coding scheme to have poor performance in weak links and may even lead to worse performance than for an uncoded signal. This is indicated in Figure 3.6 for BER higher than 10^{-2}. Figure C.24 shows the effect of the addition of the interleaver. The right figure indicates an interleaving length of 100 ms. Looking at the 2300 ms and 2500 ms, the uncoded and uninterleaved BER is just above the 10^{-2} threshold, such that coding doesn't give better performance. When interleaved, the uncoded BER decreases beneath the threshold and coding performs better.

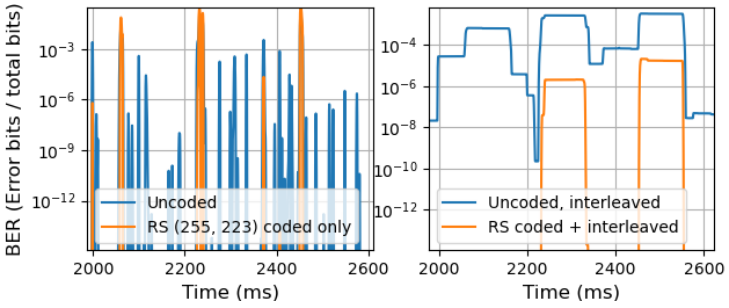

Figure C.24: BER time series uncoded (blue) and FEC coded (orange), with interleaver (right) and without interleaver (left)

C.3.6 Combined micro-scale domain

Combining all micro-scale losses with $P_{RX,0}$ gives the dynamic power P_{RX} as in Equation 3.14. Histograms of these losses, as well as P_{RX} is shown in Figure 3.5. At moderate turbulence strength, the influence of turbulence effects is comparable to platform jitter effects in terms of losses. At higher elevation angles, platform jitter is thus the most dominant effect, as expected at high cruise altitudes. Time series of both P_{RX} and BER at micro-scale are discussed in chapter 4.

C.4 Processing

Fades are verified by analyzing the statistics over a micro-scale time interval. P_{RX} is simulated at an elevation angle of 5° over an interval of 100 milliseconds in Figure C.25, where P_{RX} is the blue line and the threshold is the orange line. Fades are represented by the area below the threshold. The fading statistics computed by the model in Table C.3 show agreement with the fades observed in the P_{RX} time series in Figure C.25.

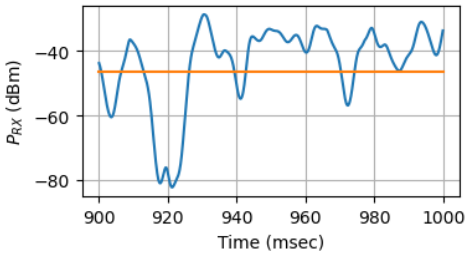

Figure C.25: Micro-scale time series of P_{RX} at 5° elevation

Fade statistics	Values
Fractional fade time	26.3%
Number of fades	4
Mean fade time	6.58 ms

Table C.3: Fading statistics for Figure C.25

The power penalty method as proposed by [52] is solely based on the scintillation. As this method is extended to all the losses that are simulated at micro-scale level, the penalty is expected to be more severe. Comparing the methods, we can see that this is indeed the case with a penalty of -60dB in Figure C.26, as opposed to a penalty of -18 dB [52] (at σ_P^2 of 1). Furthermore, Figure C.26 shows an increasingly rising penalty, while [52] shows a decreasingly rising penalty. Figure C.27 provides more insight on both matters. First, it is clear that the scintillation loss is much smaller than the jitter losses. Second, the curve of the scintillation loss indeed shows the same curve as shown in [52], indicating the same behaviour. However, the power penalty is dominated by the jitter terms.

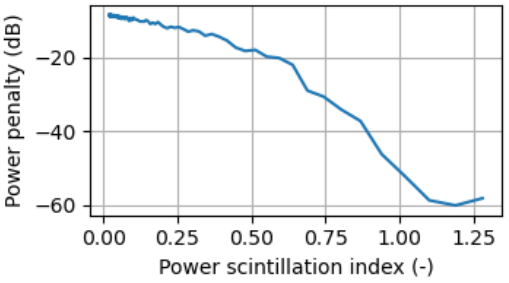

Figure C.26: Power penalty as a function of the power scintillation index

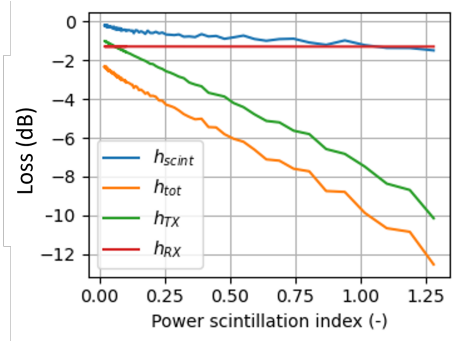

Figure C.27: All micro-scale losses as a function of the power scintillation index

C.5 Convergence analysis

For the analysis of convergence of the model, first, two test cases are defined, consisting of a constellation-aircraft combination. The constellation is the SDA tranche 0, planned to be the first operational constellation with optical uplinks and downlinks, operating in two planes at 1000 km altitude and around 80° [25]. A high-coverage and low-coverage aircraft route is chosen in order to analyze the difference in performance. These are flight routes from Oslo to Eneves (for high coverage) and from Sydney to Melbourne (for low coverage).

Then a set of input parameters are selected and a set of model parameters are selected. A prioritization of the most critical model parameters as well as input parameters is done. The selected parameters are shown in Table 3.7. Sensitivity analysis is performed by simulating the model with 4 different values for each input parameter. Convergence analysis is performed by simulating over a range of model parameter values, for each input parameter value. Three performance metrics are chosen: Fractional fade time, mean fade time and signal variance. The first two metrics are an important measure for the convergence of the fading channel and the last metric is a measure for the convergence of the total signal. A threshold of 0.5 dB is used for signal variance and 5% for the fading statistics. The results are shown in Table C.4 and Table C.5, where it is indicated for each input parameter if and when the model converges.

C.5.1 Macro-scale (time steps)

For this analysis, the micro-scale population size is set to 5 seconds (50.000 samples). Table C.4 shows that the degree of convergence is quite similar between the low-coverage and high-coverage cases. The performance metrics converge for all input parameters with the exception of D_t higher than 8cm. This can be explained by the fact that a higher D_t leads to lower divergence and a higher high mean signal power $P_{RX,avg}$, which results in fewer fades. Due to insufficient fading statistics, this metric may not converge. Furthermore, the largest possible step size, while still converging, is 6 seconds.

Plotting the results shows that the D_t has a significant impact and the turbulence cut-off frequency only significantly affects the mean fade time. This can be explained by the fact that D_t has a large impact on $P_{RX,avg}$ through the antenna gain. The cut-off frequency only influences temporal behaviour of the signal.

Table C.4: Convergence results of macro-level step size

	High coverage		Low coverage	
Perf. metric	Aperture	Turb. frequency	Aperture	Turb. frequency
Frac. fade time	All 7 sec	All 7 sec	All 6 sec	All 6 sec
Mean fade time	$>$ 8cm 7 sec	All 0 sec	$>$ 5cm 6 sec	All 0 sec
Signal variance	All $>$10 sec	All 0 sec	All $>$10 sec	All 0 sec

C.5.2 Micro-scale (Monte Carlo population size)

For this analysis, the macro-scale step size is set to 6 seconds. The signal variance converges at very low population sizes for all cases. Looking at Table C.5, the low-coverage case results in better convergence for all performance metrics. For the fading statistics, this is expected as the low-coverage case contains stronger turbulence and thus more fade samples.

Table C.5: Convergence results of micro-level population size

Perf.	High coverage		Low coverage	
metric	Aperture	Turb. frequency	Aperture	Turb. frequency
Frac. fade time	All 1 sec	All 0.5 sec	All 0.5 sec	All 0.5 sec
Mean fade time	$>$ 10cm 4 sec	None -	$>$ 2cm 0.1 sec	All 0 sec
Signal variance	All 0.5 sec	All 0.5 sec	All 0.1 sec	All 0.1 sec

Looking at the high-coverage case, the mean fade time converges poorly, likely due to the insufficient number of fades. It only converges for D_t larger than 10cm due to large enough pointing errors. and doesn't converge for any cut-off frequency. This is explained by the fact that the default D_t is set to 8cm (Table 3.2) and that the different frequencies have a large impact on the mean fade time.

To provide better insight into the degree of convergence in the high-coverage case, another simulation is performed with 5 population sizes (5s,10s,25s,50s,80s) with a turbulence frequency of 1000.0Hz and a D_t of 0.08m, seen in Figure C.28. The fractional fade time isn't significantly affected by the change in elevation and converges for all population sizes. The start of erratic behaviour ranges between 30° elevation, for 5 seconds, up to around 60°, for 80 seconds. In this region, the mean fade time greatly diverges for population sizes of 5s and 10s, corresponding to 5 to 10 fades. Increasing the population size first leads to less stability (at 10s) and then grows more stable (above 50s). However, a step size of 5s is proposed for the simulation, as the erratic region only occurs at fade fractions lower than 0.1%.

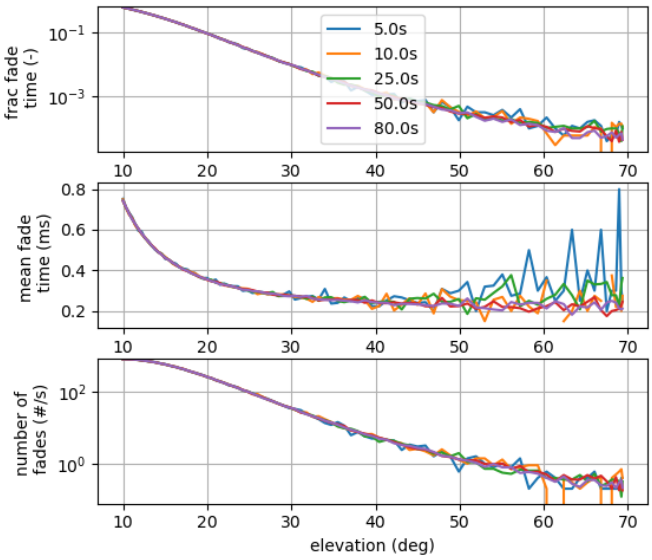

Figure C.28: Fade statistics of one link of scenario 1, plotted over its elevation range for multiple population sizes

C.5.3 Parameter selection

The prioritization performed for the selection of the most critical input parameters is shown in Table C.6. An estimated sensitivity is used as a criterion to rank the parameters. Aircraft flight route, turbulence cut-off frequency and divergence are considered the most critical input parameters (highlighted in red). First, the flight route has a large effect on the coverage, which in turn influences the performance of the entire mission. Constellation type is considered less critical in the case of mega-constellations. However, when using only a few satellites, or even one satellite at GEO, this parameter becomes more critical. Second, the turbulence frequency is estimated as a highly critical parameter, due to its large influence on the temporal behaviour. However, platform jitter may be more critical at high altitudes, where turbulence is weak. Thirdly, beam divergence has a very large impact for two main reasons. It significantly influences the transmitter gain and thus the average received signal, and it determines the magnitude of the pointing errors. A large divergence lowers the errors and vice versa.

Another prioritization is done for the selection of the model parameters. Here, two criteria are used: Sensitivity (impact) and stochastic uncertainty. These criteria are selected, because a convergence analysis is deemed more critical for model parameters with both high sensitivity and uncertainty. Table C.7 shows the ranking. The most critical model parameters are the macro-scale step size and the micro-scale population size (highlighted in red). First, the macro-scale step size ΔT likely has a very large impact, as all macroscopic variables $\mathbf{U}^T$ are propagated with Δt. The stochastic uncertainty arises from the time-discretized propagation of the satellites. Second, the micro-scale time interval is considered critical as this all microscopic variables $\mathbf{u}_t^T$ are simulated with this interval. Additionally, all variables in the Monte Carlo Power Vector tool are stochastically computed. The exact influence of the time is uncertain and therefore the stochastic uncertainty is high. The micro-scale step size δt also has a large impact. However, the value of δt (0.1 ms) is chosen such that the sampling resolution is large enough. This resolution depends on the frequency of turbulence and platform jitter, which we can already estimate quite well. Therefore, stochastic uncertainty is lower here.

Table C.6: Prioritization of input parameters that are used for the convergence analysis. Selected parameters are highlighted in red.

Aspect	Parameters	Sensitivity
LCT system	• Data rate	4
	• Wavelength	4
	• P_t	3
	• Aperture	2
	• Clipping and obsucration ratio	2
	• System temperature and load resistor	1
	• System efficiencies	3
	• BER threshold	3
Geometry	• Constellation size and type ($\bar{X}_{SC}$)	2
	• Aircraft route ($\bar{X}_{AC}$)	5
Turbulence Pointing	• Turbulence cut-off frequency	5
	• Divergence	5
	• Field-of-view	2
	• Pointing jitter	4
	• Pointing error	4
	• Platform vibration spectrum (cut-off at 100 Hz)	4
Detection & Modulation	• Detection scheme	4
	• Modulation scheme	4
	• Pre-amplification gain and noise	3
	• Bandwidth (Electrical, optical)	2
	• Focal length	2
Coding	• Coding scheme	3
	• Interleaving latency	2

Table C.7: Prioritization of the model parameters for the convergence analysis. All parameters are defined and ordered by the sub-models in which they occur. The selected parameters are highlighted in red.

Level	Sub-model	Model parameter	Sensitivity	Stochastic uncertainty	Risk score
Macro-scale	All	• Macro-scale step size ΔT	5	3	10
	SC propagation	• Integrator type	2	2	4
		• Accelerations	1	3	4
	Routing	• Optimization algorithm for link selection	3	4	7
	Atmosphere	• Attenuation profile	2	2	4
		• Cloud coverage	2	2	2
Micro-scale	All	• Micro-scale time interval	5	5	10
		• Micro-scale step size δt	5	3	8
	Platform Jitter	• Flat spectrum	3	3	6
	Turbulence	• Flat spectrum	3	4	7
		• C_n^2 profile (Hufnagel-Valley)	4	3	7
		• Wind speed profile (Bufton)	4	3	7
	MC Power vector tool	Spatial distribution for scintillation (Log-normal)	3	2	5
		• Spatial distribution for BW and AoA fluctuations (Rayleigh)	4	2	6
		• Spatial distribution for mech. jitter fluctuations (Rayleigh)	4	1	5
	Noise	• Background noise (limited to direct solar radiation)	1	0	5
	Coding	• Reed-Solomon (N,K)	2	0	2
		• Interleaver length	2	0	2

Appendix D

Parameters

This chapter covers all parameters that are used in the code of the numerical model. The input parameters that cover the hardware (LCT) constraints are listed in Table D.1 and the input parameters that make up all atmospheric and geometric constraints are listed in Table D.2. Table D.3 lists a number of additional input parameters regarding the model choices. Finally, a parameter flow diagram of all input parameters of Table D.1 and Table D.2, as well as all the simulated variables, is shown in Figure D.1.

Table D.1: Model input parameters for the hardware (LCT) constraints

	Input parameter	Unit	AC LCT	SC LCT
Optics	Wavelength	nm	1536 - 1553	1536 - 1553
	Data rate	Gb/s	2.5	2.5
	Pt	W	20	10
	Aperture diameter	mm	80	80
	Clipping ratio	-	2	2
	Obscuration ratio	-	0	0
	beam width w0	mm	20	20
	Divergence (comm)	urad	24.72	24.72
	Clipping loss	W	1.00	1.00
	Divergence (eff)	urad	24.72	24.72
	Divergence (acq)	urad	300	300
	M2 booster	-	1	1
	Focal length	cm	15	15
	Static pointing error	urad	4	4
	Dynamic pointing error	urad	3.4	3.4
	Field of View (comm)	ster	1.00E-08	1.00E-08
	Transmission loss	dB	-0.97	-0.97
	Static WFE loss	mm	100	100
	Splitting loss	-	0.9	0.9
Detection & Modulation	Optical bandwidth	GHz	2	2
	Electrical bandwidth	GHz	1	1
	Modulation scheme	-	OOK-NRZ	BPSK
	Detection scheme	-	Preamp with PIN	Preamp with PIN
	Amplification gain M	-	150	285
	Noise factor F		4	2
	Load resistor	Hz	50	50
	System temperature	K	300	300
	Quantum efficiency	-	0.8	0.8
Sensitivity	Threshold	BER	1.00E-06	1.00E-06
	Threshold	PPB	74.32	67.16
	Threshold	dBm	-45.35	-46.35
Coding	Symbol length	b/symbol	8	8
	N, K	-	255, 223	255, 223
	Interleaving latency	ms	500	500

Table D.2: Model input parameters for the atmospheric constraints and geometric constraints

	Input parameter	Unit	Value
Atmosphere	Attenuation coefficient (surface)	1/m	0.025
	Sun irradiance	W/cm2/um2/ster	0.5
	Cloud transmission		0.8
SC propagation	SC method		TLE' or 'manual'
If 'manual'	SC height	km	1000
If 'manual'	SC inclination	deg	55.98
If 'manual'	Number of planes		2
If 'manual'	Number of sats per plane		14
If 'TLE'	Filename to load		path to file
AC propagation	AC method		straight' or 'opensky'
If 'manual'	AC height	km	12
If 'manual'	AC speed	m/s	150
If 'manual'	Initial latitude	deg	35
If 'manual'	Initial longitude	deg	135
If 'opensky'	Filename to load	-	path to file

Table D.3: Model choices

	Input parameter	Unit	Value
Requirement	Max. outage probability	%	1
Numerical set-up	Macro-scale step size ΔT	sec	6.0
	Micro-scale step size δt	msec	0.1
	Step size SC propagation ΔT_{SC}	sec	7.0
	Micro-scale population size M	sec	5.0
Other	Link numer	-	'all' (or choose a number)
	Uplink or downlink	-	'up'

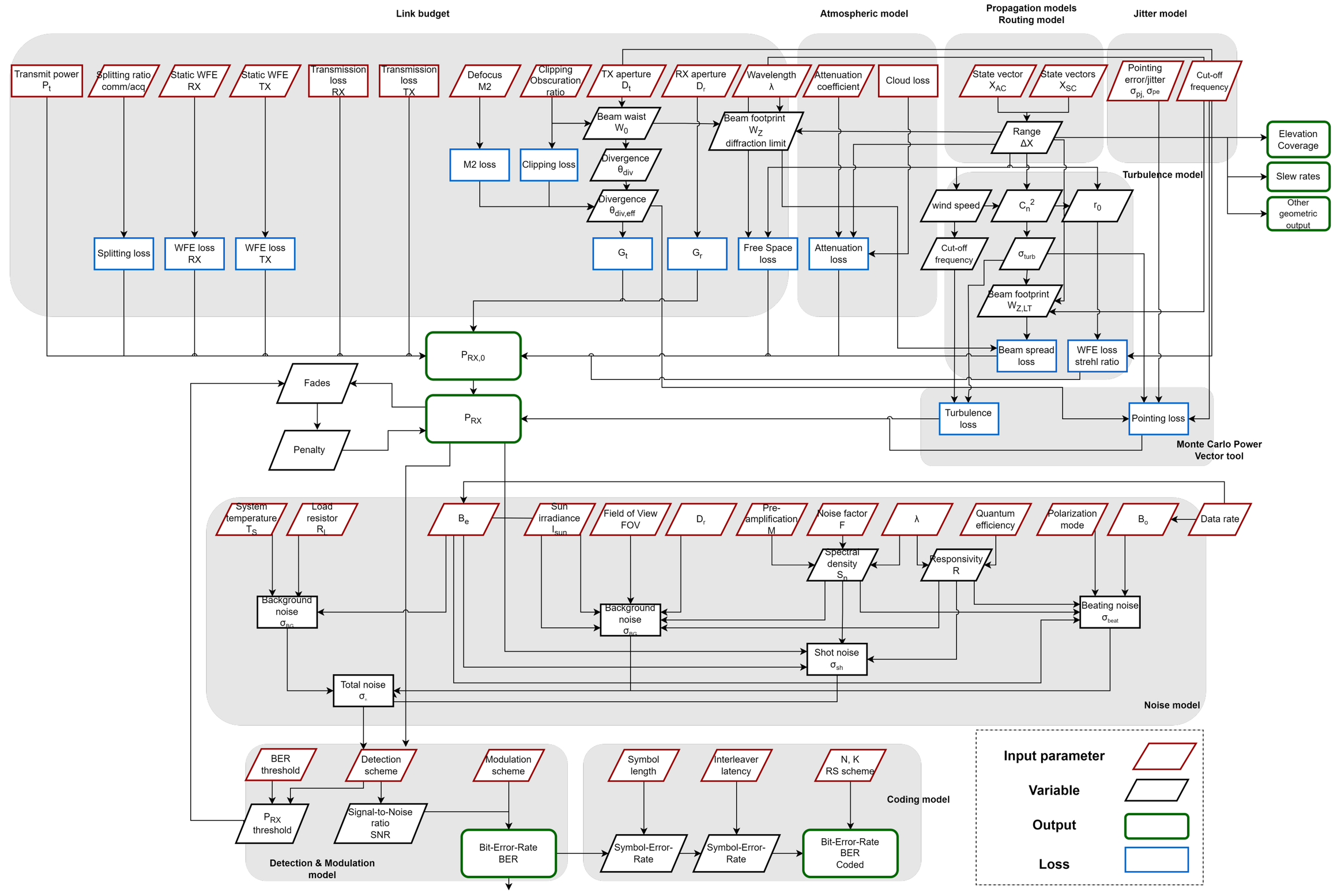

Figure D.1: Flow diagram of all parameters.

Conclusion and Recommendations

FSO communication services using LEO satellite constellations have much potential to contribute to an improvement in global internet bandwidth and connectivity. Such missions are very complex and consist of many physical processes. Firstly, there are (1) platform dynamics, with a frequency of minutes to hours. Secondly, considering a LEO constellation there is a (2) link frequency of 5 to 10 min, where atmospheric attenuation occurs. At lower time scales, (3) atmospheric turbulence and platform vibrations occur between each 1 to 100 milliseconds, and (4) bit transportation and processing occur into the order of nanoseconds. Modeling the communication performance of these missions will enable mission-level analysis and verification of these missions, and provide better insight in the complex physical behaviour. Therefore, the main objective of this thesis research was to: Develop an end-to-end model that combines all relevant processes within a global free-space optical communication mission between one aircraft and a satellite constellation.

To do this, a modified multi-scale method (MMM) is developed, derived from the Heterogeneous multi-scale method (HMM) and the Time-parallel compound wavelet method (TPCWM). With the research objectives in mind, there was a focus on accuracy, efficiency, versatility and low complexity. Sub-models are extracted from literature for modeling all the above processes, which are then combined using the MMM.

The developed end-to-end model, using the MMM, is able to realistically simulate an FSO communication service between an aircraft and a satellite constellation, while the addition of the TPCWM further increases efficiency. The model simulates a 1.5 hours communication mission in approximately 6 minutes with 8Gb RAM using a normal PC. In the case of aircraft-to-satellite links (ASL), platform dynamics and platform vibrations are the most dominant effects with respect to performance. Including microscopic processes results in a signal power difference of 10dBW to 80dBW depending on the strength of the atmospheric channel.

The model contains several limitations for which recommendations are provided. Firstly, in the micro-scale domain, this research assumes a flat power spectrum of the signal with cut-off frequencies, which is static for each microscopic evaluation. A more realistic look into the temporal behaviour of the signal requires the use of a temporal power spectrum model, such as Tatarskii, von Kármán or the modified atmospheric spectrum. Additionally, in reality each turbulence fluctuation contains its own power spectrum. Including the variation of a temporal power spectrum in the micro-scale domain would make the model more realistic, but comes with the challenge of increased computational cost. Furthermore, the current model is limited to ASL missions. Despite the versatile design, extending the model to ground-to-space (GSL) missions requires a modification of the atmospheric turbulence model and the atmospheric attenuation model, due to the addition of the lower earth's atmosphere. Furthermore, the current model uses a simplified routing model in which the optimization is solely based on geometric data. To further improve versatility, different routing methods could be implemented that optimize based on other metrics such as throughput or signal power P_{RX}. This would require the performance output of the end-to-end model to be fed back into the routing model.
Finally, in addition to the verification that is already performed, more complete verification and validation can be performed. Unit test verification of all single code functions is recommended. This research has assumed correct code functioning with successful verification of all sub-models. Additionally, complete validation should be performed with experimental measurements obtained from demonstrations, when available.